CHALMERS
UNIVERSITY OF TECHNOLOGY

Combined Empirical and 1D Modeling Approach for Exhaust Aftertreatment System for Heavy Duty Diesel Engines

Master's thesis in Innovative and Sustainable Chemical Engineering

FRIDA ALMQVIST

Supervised by
Hannes Kannisto
Jelena Andric
Jonas Sjöblom
Ethan Faghani

Department of Applied Mechanics
Chalmers University of Technology
Gothenburg, Sweden 2017

Master's thesis 2017:81

Combined Empirical and 1D Modeling Approach for Exhaust Aftertreatment System for Heavy Duty Diesel Engines

FRIDA ALMQVIST

CHALMERS
UNIVERSITY OF TECHNOLOGY

Department of Applied Mechanics
Chalmers University of Technology
Gothenburg, Sweden 2017

Combined Empirical and 1D Modeling Approach for Exhaust Aftertreatment System for Heavy Duty Diesel Engines
FRIDA ALMQVIST

Supervisor: Jelena Andric, Applied Mechanics
Supervisor: Hannes Kannisto, Volvo Penta
Supervisor: Ethan Faghani, Volvo Penta
Examiner: Jonas Sjöblom, Applied Mechanics

Master's Thesis 2017:81
Department of Applied Mechanics
Chalmers University of Technology
SE-412 96 Gothenburg
Telephone +46 31 772 1000

Cover: Catalytic muffler for the D13 engine at Volvo Penta

Typeset in LaTeX
Printed by [Name of printing company]
Gothenburg, Sweden 2017

Combined Empirical and 1D Modeling Approach for Exhaust Aftertreatment System for Heavy Duty Diesel Engines

FRIDA ALMQVIST
Department of Applied Mechanics
Chalmers University of Technology

Abstract

The aim of this project was to develop a model for the first part of the exhaust aftertreatment system including diesel oxidation catalyst (DOC) and diesel particulate filter (DPF). The model would then be tested against test cell data to evaluate if it could be used in a virtual test rig. The model consists of two individual models one for DOC and one for DPF respectively, which were later linked together. The software used was GT-SUITE and the models were constructed as 1D single channel flow and tested against test cell data provided by Volvo Penta. The key parameters of investigation were concentration of CO, HC and NO, temperature and pressure drop. The reaction kinetics and properties of the substrate were optimized to get the best fit to data. The activation energy and the pre-exponent multiplier for the reaction rate expressions were optimized based on values for an entire cycle. A major error in the model is due to inconsistent degree of conversion at high temperatures (CO, HC). So at high temperatures the model predicted high conversion (100%) and the sensitivity of the parameters decreased, however, there were also come CO slip in this region which also caused problems in the model. The model should have been optimized towards the last part of the test data, where the conversion is lower than 100%. This was out of the scope for this thesis and therefore the model includes inaccurate optimized parameters for the low temperature region of the cycle. The lower conversion in test cell data might be due to a bend in the inlet pipe causing non-uniform inlet gas flow and non-uniform temperature and a flow of reactant were the model predicts almost full conversion. Another source of inaccuracy was the unknown initial soot loading of the DPF, causing errors in pressure drop simulation. Nevertheless, the models can give a good approximation to what happens in the DOC and DPF, especially when using PLM and NRTC cycles.

Keywords: Diesel oxidation catalyst, Diesel particulate filter, Kinetic modeling, Transport resistance

Acknowledgments

I would like to thank my examiner Jonas Sjöblom who has given me great insight to analysis of test results. My supervisor Jelena Andric who has organized the project and given me notes of the report. My supervisors at Volvo Penta, Hannes Kannisto and Ethan Faghani whom have given me much of the data to start the project and feedback. I would also like to thank Gamma technology, EATS team at Penta, Adrian, Måns and Carin for support during the project. The author also wish to thank and acknowledge the support contributed by Fordonsstrategisk Forskning och Innovation (FFI) and Vinnova. This manuscript was written as a part of Virtual Engine Calibration (VirCal) project funded by FFI.

Frida Almqvist, Gothenburg, September 2017

Contents

1 Introduction

This project is an initiative by Volvo Penta, to model the aftertreatment system of heavy duty diesel engines by a semi physical approach (empirical and 1D gas exchange model). The industrial goal of achieving lower emissions and higher efficiency, needs not only better understanding of new technologies but also a faster model development process in order to test new equipment. The model was constructed in GT-SUITE application from Gamma Technology. This thesis project constitutes a part of powertrain model development using a semi-physical approach. The purpose of the project is to evaluate if models developed only by input from test cell data and manufacturer data e.g. substrates are accurate enough to be used in model-based calibration process e.g. Virtual Test Cell. The leadtime of the model should be short so the models can be prepared on time for the joint virtual-physical projects. Thus a more complex model is not the goal but the evaluation if a 1D model is sufficient for predicting outcome of DOC and DPF is the main objective. This thesis is performed as part of a virtual calibration project with the goal to increase the share of modeling and simulation in engine development process.

2 Background

The reason for the interest of diesel engines are their high efficiency and low operating cost, making them a perfect fit for trucks and other heavy machinery used daily. The transport industry is governed by legislations on the amount of emissions the engines are allowed to emit. It is these legislations that govern the target on aftertreatment capacity to clean the emissions from the engine. With new legislation permitting lower emissions, new techniques have to be developed and with new designs comes testing. Test rigs where the performance of engine and catalytic muffler are measured are expensive. A virtual test rig would be a solution to get more tests faster and cheaper than real measurements. Simulation models employed in the virtual test rig have to be fast and accurate enough to form a basis for decision making on the design development of the catalytic muffler.

Diesel engines contribute to heavy pollution. Emissions from diesel engines include, carbon monoxide CO, hydrocarbons HC and oxides of nitrogen NO_x. Diesel engines also emit significant levels of particulate matter PM, which can be divided into carbonaceous soot and soluble organic fraction, SOF. Diesel particulate matter is harmful to human health and has a negative environmental impact and is therefore important to minimize (Fino, 2006). Compared to gasolene engines, diesel engines also emit higher levels of oxygen O_2 used to oxidize NO, CO, HC and soot since the engine is run on an oxygen excess (Sampara et al., 2007).

After the engine the exhaust gas flows to the catalytic muffler, where the emissions produced by the engine are cleaned. A catalytic muffler typically includes four different parts, a diesel oxidation catalyst (DOC), a diesel particulate filter (DPF), a selective catalytic reduction catalyst (SCR) and an ammonia slip catalyst (ASC) (Ratcliff A et al., 2010). In this project the muffler has two parallel SCRs and ASCs as shown in Figures (1) and (2). The models will be conducted according to the linear flow chart in Figure (2).

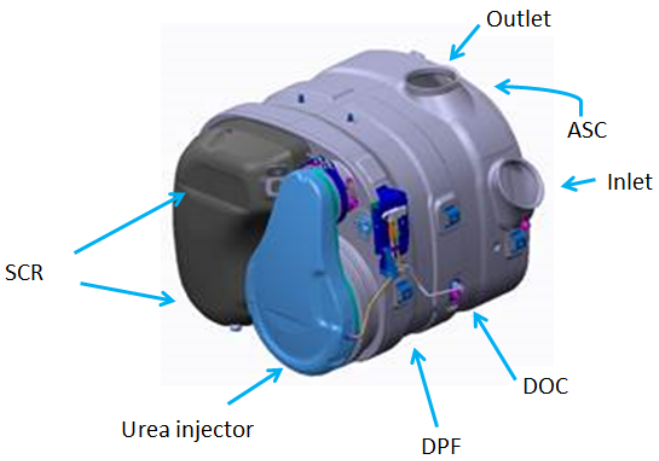

Figure 1: An illustration of the catalytic muffler and its parts

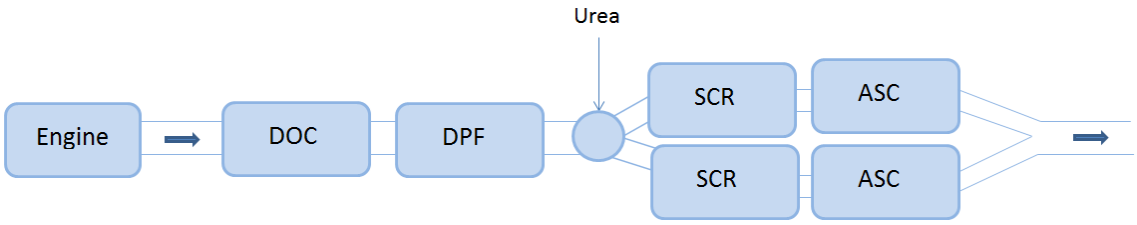

Figure 2: Flow path through the catalytic muffler. The flow first enters the DOC after the engine and thereafter the DPF. After the urea input the flow is divided into two parallel SCRs and ACSs

European emission standards for non-road diesel engines were first introduced in 1997 with the Stage I/II legislation. In 2014 the Stage V regulations where presented and they not only required lower emissions of CO, HC, NO_x and PM than their predecessors but also introduced regulations regarding particle number PN, seen in Table (1) (Dieselnet, 2017). PN is the number of solid particles the engine emits. It is these legislations that are the minimum goal of exhaust aftertreatment developers today. Comparing the emission legislation for the highest net power in Table (1) with the Stage VI regulations for heavy duty diesel engines for trucks (Dieselnet, 2017) the non-road emissions are higher.

Table 1: Stage V legislation for non-road diesel engines. a = $HC+NO_x$, b = 0.6 for hand-startable, air-cooled direct injection engines, c = 1.1 for gas engines, d = 6 for gas engines (Dieselnet, 2017)

Net Power kW	CO	HC	NO_x	PM	PN 1/kWh
	g/kWh				
P < 8	8		$7.5^{a,c}$	0.4^{b}	-
$8 \leq P < 19$	6.6		$7.5^{a,c}$	0.4	-
$19 \leq P < 37$	5		$4.7^{a,c}$	0.015	10^{12}
$37 \leq P < 56$	5		$4.7^{a,c}$	0.015	10^{12}
$56 \leq P < 130$	5	0.19^{c}	0.4	0.015	10^{12}
$130 \leq P \leq 560$	3.5	0.19^{c}	0.4	0.015	10^{12}
P > 560	3.5	0.19^{d}	3.5	0.045	-

2.1 Diesel Oxidation Catalyst (DOC)

The purpose of the DOC is to oxidize HC and CO to carbon dioxide (CO_2) and water. Another purpose is to oxidize nitric oxide NO to nitrogen dioxide NO_2, since NO_2 is used as an oxidation agent for the soot in the DPF. NO is an odorless and colorless gas, NO_2 is a very toxic gas that has an irritating odor and is extremely reactive. The result of NO_x emissions in the atmosphere are fertilization and acidification of water and soils, but also human respiratory disorders. About 40% of the NO_x emissions originate from transport sources resulting in actions taken towards NO_x control (Naturvårdsverket, 2017). The HC in the exhaust gas originates either from lubricating oil or the fuel as decomposed fuel molecules or intermediate compounds (Majewski and Khair, 2006). The long chained HC often have a characteristically irritating odor and can be both toxic and carcinogenic. CO is just as NO, an odorless and colorless gas. CO is very toxic and can be flammable at high concentrations. The oxidation reactions in the DOC are exothermic which means that after a certain temperature is reached the reaction should be self-sustained, however this excess heat is transferred along the gas since, since the concentrations are low, or lost due to heat losses in the walls, so the temperature does not increase uncontrollably. The oxidation of CO is the most important contributor to the raise in temperature (Majewski and Khair, 2006) (Ye et al., 2011) (Wang-Hansen, 2012). An illustrative picture of incoming and outgoing substances in

the DOC can be seen in Figure (3). Since the conversion at low temperatures is often not 100%, the inlet species will also be present in the outlet stream.

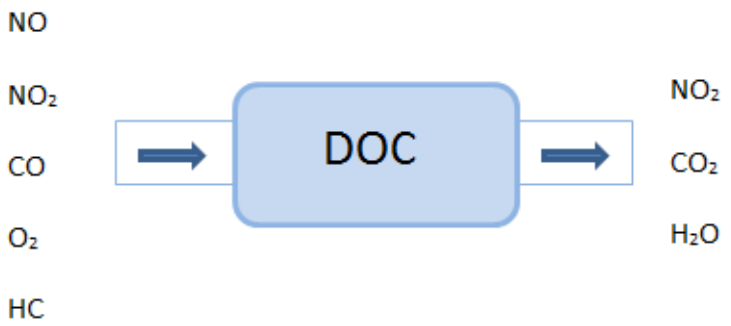

Figure 3: The inlet and outlet species composition of DOC

2.2 Diesel particulate filter (DPF)

Diesel particulate matter is one of the most harmful emissions produced. The measurement of PM is done by a sampling method, where a sample of the exhaust is filtered to get a measure of mass of the PM. This is done since soot is not a well-defined chemical species. These particles are categorized into three subgroups, SOL, SOF and SO_4. Solid fraction, SOL, includes elemental carbon and ash. Soluble organic fraction, SOF, includes organic material and sulfate particulates. SO_4 is aqueous sulfuric acid (Majewski and Khair, 2006) (Andersson, 2006). The PM is collected by a filter, the DPF, and in order to get the highest amount of PM collected and prevent a raise in pressure drop by soot blocking the filter channels, the filter needs to be cleaned, which is called regeneration (Andersson, 2006) (Wang-Hansen, 2012). The regeneration can be performed in two ways, either with a passive or active filter. The passive filter is continuous, where a catalyst lowers the energy needed for the oxidation so that the heat from the exhaust gas is sufficient to activate the reactions. The active filter uses an external heat source to oxidize the soot (Majewski and Khair, 2006). PM spontaneously burns in air but at temperatures around $600°C$. The regeneration of the filter used in this study, is done in the first way mentioned above, by lowering the ignition temperature of the soot by other substances, which catalyzes the soot oxidation. By using a catalyst in the DPF, tests have showed that it not only accelerates the oxidation step, but also prolongs the trapping of the soot period (Fino, 2006). The PM is oxidized with NO_2, produced in part by the DOC, and O_2, where NO_2 is the stronger oxidizer (Fino, 2006). To get the highest conversion in the SCR, a 50% mixture of NO and NO_2 is a favorable output from the DPF (Sampara et al., 2007). By coating the DPF with platinum group metals, such as platinum and palladium, NO can once again be oxidized to NO_2, making it possible to reach the 50% target and still oxidize as much soot as possible. Figure (4) illustrates the inlet and outlet species from the DPF. If the conversion is less than 100%, the output stream would consist of some of the inlet species as well.

Figure 4: The inlet and outlet species composition of the DPF

2.3 Selective Catalytic Reduction (SCR) and Ammonia Slip Catalyst (ASC)

In the SCR the NO_x is reduced into N_2 and H_2O over a catalyst. Urea is injected into the stream and consists of aqueous solution of ammonia that decomposes into free ammonia, NH_3, when mixed with the hot flue gases. The mixing pipe is constructed to be long enough to ensure sufficient mixing between the urea and the flue gases. The reactions in the SCR are endothermic and thereby dependent on the temperature, which is lowered when the urea is mixed with the gas. The low-temperature SCR reactions are then no longer governed by the rate of mass transfer but rather by the rate of chemical reaction. This is a present issue for many manufacturers that want to use the excess heat in the exhaust gases to increase the efficiency of the engine and still reduce NO_x emissions (Johnsson, 2011). The final step, the ASC, oxidizes leftover NH_3 that has not been used in the SCR and turn it into N_2 and H_2O. Figure (5) illustrates the inlet species of the SCR and the outlet species from the ASC which enters the surrounding atmosphere.

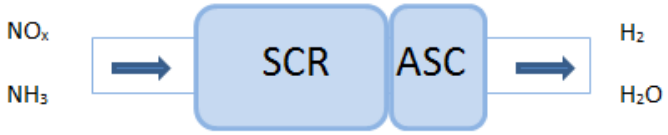

Figure 5: The inlet and outlet species composition of the SCR + ASC

2.4 Project Scope

The scope of this project is on DOC and DPF simulation. First, the focus is the DOC alone then the DPF alone. This choice is made to prevent that the inherited DOC simulation errors are included in the DPF simulations. Finally, the DOC- and the DPF models are combined, however, the combined model has not been further optimized. The modeling and validation of SCR and ASC is out of the scope of this project since it would require a longer time frame of the project.

3 Theoretical and Modeling Background

3.1 Catalytic Reactors

A catalyst is a species that can increase a reaction rate without being consumed. Without catalysts, many reactions would not be feasible to handle in industrial applications. The catalyst can be homogeneous i.e. same phase as reactant, or heterogeneous i.e. different phase from the reactant (Busca, 2014). In the catalyst of exhaust aftertreatment the catalysts are solid metals mixed in a washcoat that is coated on a monolith, a cordierite structure, designed for high area exposure towards the exhaust gas, creating a porous layer (Aberg et al., 2016). These platinum group metals, PGM, are refered to as sites, where the reactive species absorb, react with for example, the oxidizer to the product species, and then desorb back to the gas. The metals are not consumed in the reaction, they act as a medium to lower the energy level the reactants need to overcome in order to react and hence speed up the reaction (Lohse, 1945). Figure (6a) illustrates the cordierite structure. The porosity of the washcoat and the PGM sites are seen in Figure (6b).

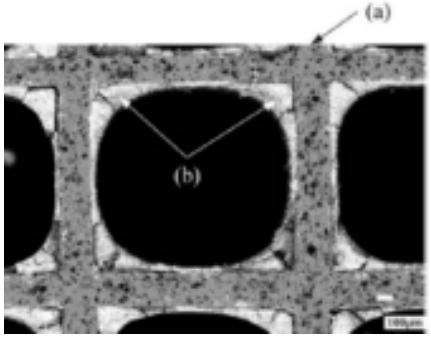

(a) Picture of coated channels of washcoat in a cordierite structure, a channel is typically 1 mm wide, (Zhang et al., 2004)

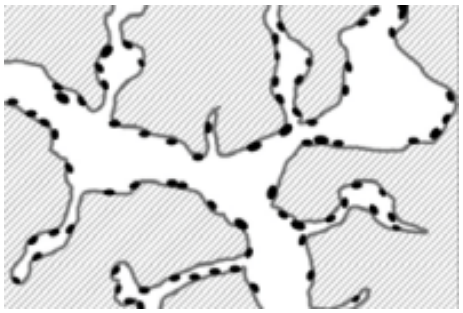

(b) A schematic image of porous channels in washcoat with PGM sites, were a pore is typically 15μm wide (Creaser, 2017)

Figure 6: Coated structure with catalytic washcoat

3.2 GT-SUITE

GT-SUITE, developed by Gamma Technologies, is a simulation software for 0D, 1D and 3D multiphysics systems. It is based on a set of component libraries which simulate fluids, thermal changes, electrics, chemistry etc. GT-SUITE does not only simulate properties of the engine but also the exhaust aftertreatment system (GammaTechnologies, 2017*b*) . The motivation for GT-SUITE as a simulation tool for this project is based on previous projects in engine simulation done in GT-SUITE at Volvo Penta.

3.2.1 Mass and heat transport

The flow in the substrate channels is solved with a quasi-steady state solver, QS solver. The recommended reaction solver is the advanced adaptive solver presented in GT-SUITE by Gamma Technology. These solvers uses the mass, heat and momentum reactions (2) - (4) and (6) below. The residence time in the substrate and channels is short compared to other time scales like driving

cycle. Due to this short residence time the substantial derivative in all gas phase equations can be replaced with a simpler derivative based on axial length according to Equation (1).

$$\frac{D}{Dt} \rightarrow \upsilon \frac{\partial}{\partial z} \tag{1}$$

The catalyst is divided into axial parts by the discretization length which the user determines, according to Figure (7). This length divides the brick into a uniform axial mesh were mass and heat equations are solved before entering the next axial part, illustrated by the thin and thick arrows respectively in Figure (8).

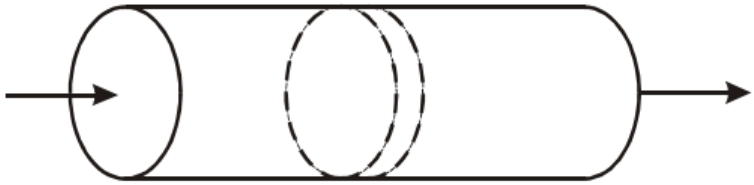

Figure 7: Scematic image describing how monoliths are divided into several axial discretization lengths

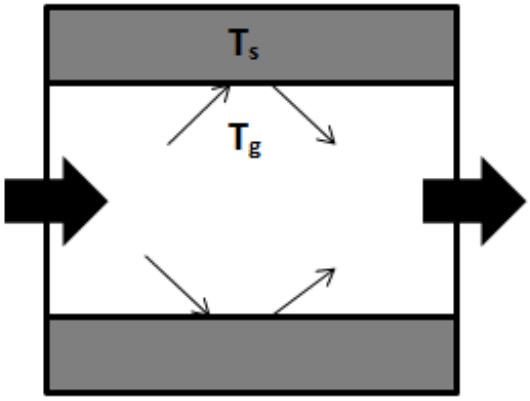

Figure 8: A schematic image of one discretization length. The thin arrows illustrates the heat and mass exchange between the gas and the washcoat. The thick arrows illustrates the transport to and from the adjacent discretization boxes. T_s and T_g are the temperatures in the solid phase and gas phase respectively

The mass transport in every discretization part is diffusion of reactants and products between the gas phase and the solid. The external diffusion in Figure (9), includes convective transfer from the bulk through the film to the surface of the particle (1,2). The internal diffusion refers to the pore diffusion inside the porous structure (3). On the active site, the reactant adsorbs, reacts and the product desorbs (4,5).

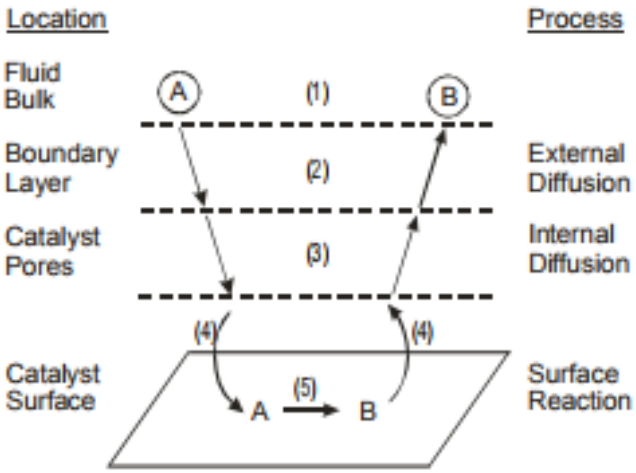

Figure 9: Diffusion from bulk to catalyst, reaction on catalyst surface and diffusion from catalyst to bulk.

The mesh solutions from every discretization length, called the method-of-lines, MOL produces the solid phase wall temperature T_s and coverage equations. The coverage refers to the empty sites of the washcoat where the reactions occur. Some substances do not absorb to a site or absorb and desorb so fast that this steps can be neglected. In this model a part of the hydrocarbons are the only species which absorb to the washcoat.

The concentrations and temperature of the gas phase T_g, depend on the MOL solution output, T_s and coverage. The gas phase equations, solving concentration and T_g are lumped together and form a system of differential-algebraic equations, DAEs, along the axial direction. These are solved by a time step integrator, LSODI (Lagrangian Implicit Ordinary Differential Equations System). The concentrations and gas phase temperature are solved for each axial part of the catalyst before entering the next part.

The energy balance, illustrated in Figure (8), for the solid phase is described in Equation (2). The different terms are in order left to right an accumulation-, diffusion-, convective heat transfer-from the bulk gas to the catalyst surface, reaction energy-, power input- and the convective heat transfer term from the external phase to the catalyst surface. Equation (3) represents the energy balance in the gas phase, with an accumulation term on the left hand side of the equation and a diffusion term on the right hand side. The mass balance is described by Equation (4), with an accumulation, diffusion and reaction term. The symbols in Equations (2) to (6) are described in Table (2).

$$\Psi_s \frac{\partial T_s}{\partial t} = \frac{\partial}{\partial z}(f_{sb}\lambda_{sb}\frac{\partial T_s}{\partial z}) + hS(T_g - T_s) - \sum_{j=1}^{nrct} \Delta H_j r_j + \frac{P}{V} + h_x S_x (T_x - T_s), \tag{2}$$

$$\varepsilon \rho_g \upsilon C_{pg} \frac{\partial T_g}{\partial z} = hS(T_s - T_g), \tag{3}$$

$$\varepsilon \rho_g \upsilon \frac{\partial \omega_g}{\partial z} = k_{m,i} S(\omega_{s,i} - \omega_{g,i}) = \sum_{j=1}^{N} \sigma_{i,j} r_j. \tag{4}$$

Table 2: Symbols of the mass-and heat transfer equations

Ψ_s	Effective hear capacity [J/m^{3}K]
T_s	Temperature of gas at catalyst surface - solid phase temperature [K]
z	axial length [m]
f_{sb}	Solid fraction of substrate
λ_{sb}	Thermal conductivity of substrate [J/m s K]
h	Heat transfer coefficient [W/m^{2}sK]
S	Surface area per reactor volume [m^{-1}]
T_g	Temperature of bulk gas in reactor channels [K]
ΔH_j	enthalpy of reaction j [J/mol]
r_j	Reaction rate of reaction j [mol/m^{3}s]
P	Power input [J/s]
V	Reactor volume [m^3]
h_x	External heat transfer coefficient [W/m^{2}K]
S_x	External surface area per reactor volume [m^{-1}]
T_x	External temperature [K]
ε	Void fraction of reactor
ρ_g	Density of bulk gas in reactor channels [kg/m^3]
υ	Velocity [m/s]
C_{pg}	Heat capacity of gas [J/kgK]
$\omega_{g,i}$	Mass fraction in bulk phase of species i
$k_{m,i}$	Mass transfer coefficient for trace species i [kg/m^{2}s]
$\omega_{s,i}$	Mass fraction at the surface of species i
N	Total number of reactions
σ_i	Stoichiometric coefficient of species i
f_f	Friction factor

Equations (5) and (6) represents the continuity of density and velocity in the axial direction, and the momentum difference, respectively i.e.

$$\frac{\partial}{\partial z}(\rho_g \upsilon) = 0, \tag{5}$$

$$\varepsilon \frac{\partial p}{\partial z} + \epsilon \rho_g \upsilon \frac{\partial \upsilon}{\partial z} = -S f_f \frac{1}{2} \rho_g \upsilon^2. \tag{6}$$

The molar flux from the bulk to the surface of the particle are defined according to Equation (7), were $k_{m,i}$ is the mass transfer coefficient for species i. This describes the film model were an imaginary film is placed between the two phases and a gradient in of the concentration can arise due to mass transfer resistance between the bulk phase and the surface. The mass transfer coefficient is determined by the Sherwood number Sh (Welty et al., 2008).

$$N_i = k_{m,i}(C_{A,bulk} - C_{A,surface}). \tag{7}$$

The Nusselt number Nu and Sherwood number are defined according to Equation (8) and (9), respectively. The Nusselt number describes the heat transfer while the Sherwood number is coupled with the mass transfer. Both numbers depend on the geometry of the substrate and Reynolds number Re as well as the Prandtl number for Nu and the Schmidt number for Sh. Re is calculated according to Equation (10). Looking at the equation for Sh it depends on the geometry by the hydraulic diameter of the channel D_h and the fraction between the mass transfer coefficient and

the diffusivity coefficient. An increase in Sh number would decrease the mass transfer resistance which is the inverse of the mass transfer coefficient.

$$Nu = D_h \frac{h}{\lambda_g}, \tag{8}$$

$$Sh = D_h \frac{k_{m,i}}{\rho D_{i,m}}, \tag{9}$$

$$Re = \frac{D_h \rho \upsilon}{\mu}. \tag{10}$$

Since the channels are so small, the flow inside the channels is assumed to be laminar and fully developed. The coated channels are also assumed to be squared, thus a uniform layer of washcoat. Nu, Sh and $f_f R_e$ can therefore assume the values in Table (3).

Table 3: The constant values used in the model for Nusselt number, Sherwood number and friction factor multiplied with Reynolds number

Nusselt number	2.98
Sherwood number	2.98
$f_f R_e$	14.24

3.2.2 Reaction Rates

Since the reactions over the PGM are faster than the storage of HC in the washcoat, they are modeled as global reactions. This means that they do not take the storage into account when calculating the rate of reaction since the adsorption and desorption are so fast that they can be neglected, as mentioned above.

Equation (11) describes the general rate expression used in GT-SUITE, where β is the order of the concentration term. The inhibition functions, G, are different for each reaction, to include specific properties of that expression, for example the reversibility of the NO oxidation. The rates of the reactions are dependent not only on concentration and temperature but also on the coverage of the respective site element. The reaction constant, k, is expressed as Equation (12), where F is the pre-exponent multiplier, E_a is the activation energy, R and T are the gas constant and temperature, respectively. k is not to be mixed with $k_{m,i}$ which is the mass transfer coefficient (GammaTechnologies, 2017a).

$$r = kC^{\beta}(G), \tag{11}$$

$$k = Fexp(\frac{-E_a}{RT}). \tag{12}$$

The active site density a_j is handled as a multiplier to each rate and can be calculated according to Equation (13).

$$a_j = \frac{(PGMLoading)(Dispersionfactor)}{AtomicWeight}. \tag{13}$$

By combining the Equations (11) to (13) an expression for the change in coverage, Equation (14) is formed for a specific reaction. A_k is the active site density for coverage and θ is the coverage.

$$A_k \frac{d\theta_k}{dt} = \sum_j \sigma a_j F exp(\frac{-E_a}{RT}) C^{\beta}_{reactant} G_i. \tag{14}$$

3.2.3 Diffusion

If diffusion is not accounted for in the model, the gas phase and the surface species have the same concentration making the kinetics the only governing reaction driving force. Since the default installations in GT-SUITE are chosen for pore diffusion in the DOC, the effective diffusivities are calculated using Equation (15). If the default installations are not chosen, effective diffusion resistance for each trace species must be entered into the model.

$$\frac{1}{D_{eff}} = \frac{\tau}{\epsilon}(\frac{1}{D_{gas}} + \frac{1}{D_{Kn}}) \qquad\qquad D_{Kn} = f(d_{pore}). \tag{15}$$

When pore diffusion is considered, the reaction rate in the solid phase energy equation is replaced by the average reaction rate over the washcoat thickness, on the assumption that the site densities are distributed uniformly, Equation (16). The washcoat thickness, δ is defined as the fraction of the solid fraction of washcoat, f_{wc} to the surface area per reactor volume.

$$\overline{r_j} = \frac{1}{\delta} \int_0^{\delta} r_j dx. \tag{16}$$

The internal mass transport inside the washcoat is defined according to Equation (17). Where the rate of the species is expressed as Equation (18).

$$f_{wc} \rho_s D_{e,i} \frac{\partial^2 \omega_i}{\partial x^2} + R_i = 0. \tag{17}$$

$$R_i = M_i \sum_j a_j \sigma_{i,j} r_j. \tag{18}$$

3.2.4 Optmization algorithms

Two of the optimization algorithms in GT-SUITE are the generic- and simplex algorithms (GammaTechnologies, 2017*a*). When using three or more independent parameters the generic algorithm is recommended. The inputs are population size and number of generations, the multiplicity of them gives the number of iterations for that optimization run. The optimizer will not stop until all of the iterations are complete. The simplex algorithm is a local optimizer and will converge to a local minimum, thus is not suitable for multiple-modal problems. The inputs for the simplex

algorithm are resolution in % (usually 1 - 3%). If n is the number of independent variables, simplex algorithm starts by creating an initial simplex consisting of n+1 solutions. After the initial simplex the algorithm proceeds by running a single iteration at a time.

3.3 DOC

The DOC used for the non-road 13 L diesel engine at Volvo Penta seen in Figure (10) has a diameter D and length L. The washcoat consists precious group metals PGM.

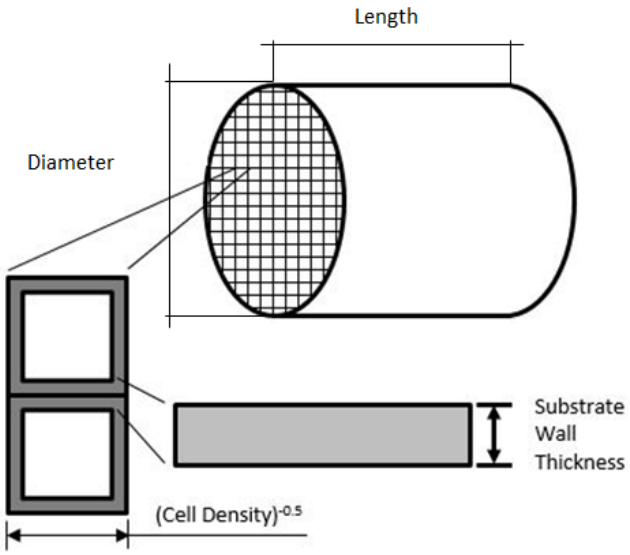

Figure 10: Diesel oxidation catalyst with square channels and set geometry

3.3.1 Flow

In the DOC model the flow solver used is the recommended QS solver described above. The time step is an important parameter in the model. According to the GT Exhaust Aftertreatment Application Manual the time step size should be less or equal to the frequency of the measured data. The chemistry solver used in the model for the DOC is the recommended Advanced Adaptive solver.

The reaction rate is chosen to be based on site (turnover number). It is a normalized basis and defined as moles reacted per moles of active sites per second. The flow is assumed to be laminar and the channels are squared resulting in values taken from Table (3) for the dimensionless numbers.

3.3.2 Reactions

The main reactions occurring in the DOC are oxidation reactions of CO, NO, $Dieselfuel$, H_2 and C_3H_6, defined below. Propylene, C_3H_6 represents the fast oxidizing part of the hydrocarbons, HCs. Reaction (21) refers to the oxidation of the unburnt diesel fuel, assumed to be 50% of the original HCs (GammaTechnologies, 2017a). The oxidation rate of CO is faster than the rate for HC oxidation but both should have high conversion at high temperatures (Sampra et al., 2008).

$$CO + \frac{1}{2}O_2 \rightarrow CO_2 \tag{19}$$

$$NO + \frac{1}{2}O_2 \rightarrow NO_2 \tag{20}$$

$$Dieselfuel + 19.4O_2 \rightarrow 13.5CO_2 + 11.8H_2O \tag{21}$$

$$H_2 + \frac{1}{2}O_2 \rightarrow H_2O \tag{22}$$

$$C_3H_6 + 4.5O_2 \rightarrow 3CO_2 + 3H_2O \tag{23}$$

The NO oxidation expression, Equation (20), is reversible resulting in a different inhibition function compared to the ones for CO and HC, below. Along with the inhibition function for the NO oxidation, the reaction rate also needs an expression to convert the rate from equilibrium to calculated, defined as the last two rows in Table (4).

Table 4: The inhibition functions for the oxidation reactions

G(1)	CO-inhibition;	$(1 + 248 \cdot exp(\frac{-614.9}{T})[CO])^2$
G(2)	HC-inhibition;	$(1 + 20^{-17} \cdot exp(\frac{2.823 \cdot 10^4}{T})([HC_{ad}] + [HC_{vap}]))^2$
G(3)	NO-inhibition;	$1 + 0.242 \cdot exp(\frac{4861}{T})[NO]$
G(4)	$Conversion\ factor\ from\ K_{eq}\ to\ K_c$;	$\sqrt{\frac{101325}{R \cdot T}}$ $[(mole/m^3)^{0.5}]$
G(5)	$NO\ oxidation\ equilibrium\ constant\ K_{eq}$;	$1.5{\cdot}10^{-4} \cdot exp(\frac{6864}{T})$

Equations (24) to (27) describes the reaction rates for the oxidation reactions of CO, NO and HC.

$$r_{CO} = k_{CO}\frac{[CO] \cdot [O_2]^{0.5}}{G(1)G(3)} \tag{24}$$

$$r_{NO} = k_{NO}\frac{([NO] \cdot [O_2]^{0.5} - [NO_2])G(4)}{G(2)G(3)G(5)} \tag{25}$$

$$r_{Propylene} = k_{Propylene}\frac{[Propylene] \cdot [O_2]}{G(1)G(3)} \tag{26}$$

$$r_{Dieselfuel} = k_{Dieselfuel}\frac{[Dieselfuel] \cdot [O_2]}{G(1)G(3)} \tag{27}$$

3.4 DPF

The channels in the DPF are different from the other substrate. They have a plug at half of the inlet and the other half at the outlet, in this way the gas has to flow through the porous wall in order to exit the DPF (Hidemitsu and Shuichi, 2008) according to Figure (11a). Figure (11b) is a more demonstrative image of how the gas flow has to penetrate the porous wall.

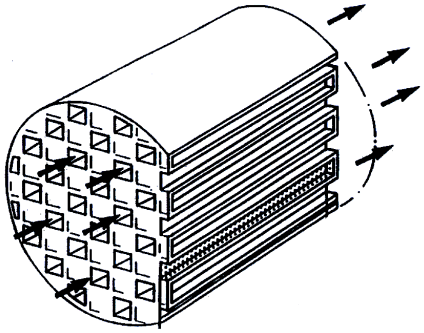

(a) DPF with gasflow indicated by arrows

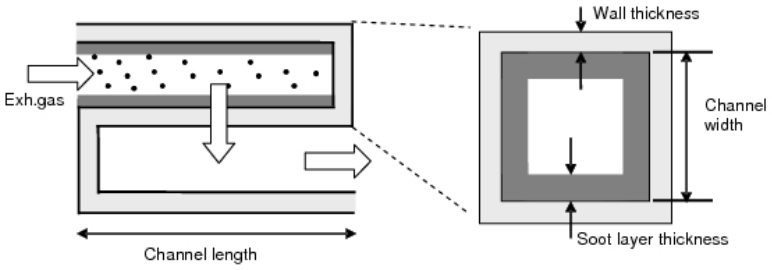

(b) Gasflow through filter and cross section of one tube

Figure 11: DPF geometry and gasflow path

3.4.1 Flow

In the DPF model the QS solver was used as the flow solver and the advanced adaptive solver was used to solve the chemical reactions. The flow is assumed to be laminar and the channels are square resulting in values taken from Table (3) for the dimensionless numbers.

3.4.2 Reactions

The soot in the DPF is oxidized according to Equation (28) to (31). Since the DPF is coated with precious metals Equation (19) to (23) are also active in the washcoat of the DPF but not in the soot cake layer.

Equation (28) and (29) describes the passive regeneration while Equation (30) and (31) the active regeneration. The major difference are the reactants to oxidize the soot, C and the temperature interval where the reactions take place. The reaction rate is just as the DOC model, chosen to be based on site (turnover number).

$$C + NO_2 \rightarrow CO + NO \tag{28}$$

$$C + 2NO_2 \rightarrow CO_2 + 2NO \tag{29}$$

$$C + 0.5O_2 \rightarrow CO \tag{30}$$

$$C + O2 \rightarrow CO_2 \tag{31}$$

The inhibition functions for the soot oxidation reactions are the selectivity factors between the CO and the $CO2$ oxidation according to Equation (32) where SF stands for selectivity factor. The inhibition functions and reaction rate expressions for the oxidation reactions of CO, NO and HC are the same as for the DOC model, see Table (4) and Equations (24) to (27).

$$SF_{CO} = 1 - SF_{CO_2} \tag{32}$$

3.4.3 Permeability

Permeability is a measure of how well the material is penetrable by the external phase, here gas through filter. If the clean filter permeability is unknown for the DPF, it is calculated according to Equation (33), based on the void fraction and diameter. If the permeability is zero in the DPF then the gas cannot flow through, causing stop in the muffler and high back pressures. The product of soot layer density and soot layer permeability depends on engine type, injection pressure, filter type, operation point, fuel additives, etc. (Stratakis et al., 2002).

$$\kappa_{clean} = \frac{\varepsilon^3 d^2}{180(1-\varepsilon)^2}. \tag{33}$$

3.4.4 Pressure drop

The pressure drop over the DPF can be divided into six different pressure drops all summarized into one total pressure drop, according to Figure (12). All ΔP_i are described in Table (5).

$$\Delta P_{total} = \Delta P_1 + \Delta P_2 + \Delta P_3 + \Delta P_4 + \Delta P_5 + \Delta P_6$$

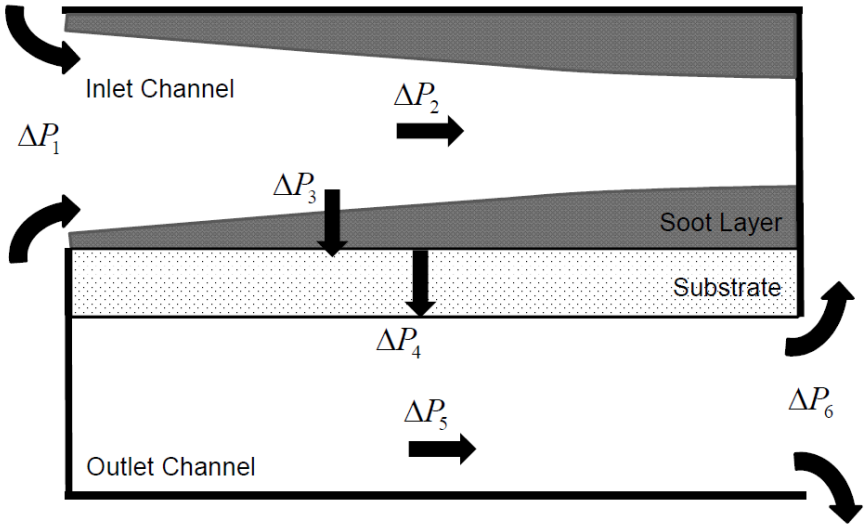

Figure 12: All contributing pressure drop locations to the total pressure drop over the DPF

Table 5: The different contribution to overall pressure drop in DPF, were the symbols are explained in Table (6)

ΔP_i	Pressure drop due to	Calculated according to
ΔP_1	Contraction	$= \frac{\xi_{contraction}\rho_{inlet}\upsilon_{inlet}^2}{2}$
ΔP_2	Friction in inlet channel	$= \frac{\mu Q}{2V_{trap}}(D+w_{wall})^2\frac{4HL^2}{3}(\frac{1}{(D-2w_{soot})^4})$
ΔP_3	Soot cake layer	$= \frac{\mu\upsilon_{w,1}(D-2w_{soot})}{2\kappa_{soot}}ln(\frac{D}{D-2w_{soot}}) + \alpha_{soot}\rho w_{soot}\upsilon_{w,1}$
ΔP_4	Filter wall	$= \Sigma_i(\frac{\mu\upsilon_{w,2}w_{slab,i}}{\kappa_{wall,i}} + \alpha_{wall}\rho w_{slab,i}\upsilon_{w,2}^2)$
ΔP_5	Friction in outlet channel	$= \frac{\mu Q}{2V_{trap}}(D+w_{wall})^2\frac{4HL^2}{3}(\frac{1}{D^4})$
ΔP_6	Expansion	$= \frac{\xi_{expansion}\rho_{outlet}\upsilon_{outlet}^2}{2}$

Table 6: Symbols of the calculations for pressure drop

ξ	Pressure drop coefficient
Q	Volumetric flow rate [m^3/s]
w_{wall}	wall layer thickness [m]
w_{soot}	soot cake layer thickness [m]
$w_{slab,i}$	Thickness of each discretization slab in the DPF layer [m]
D	Channel width [m]
α_i	Forchheimer constant in layer i [1/m]
H	Channel pressure drop correlation = 28.454
L	Channel length [m]
V_{trap}	Total filter volume [m^3]
$\upsilon_w, 1$	Velocity at soot layer inlet [m/s]
$\upsilon_w, 2$	Velocity at substrate wall [m/s]

3.5 Test Cycles

The different cycles used to produce test cell data and used to model and validate these models are part load map (PLM), non-road transient cycle (NRTC) and the non-road steady-state cycle (C1). The part load map starts with running the engine at high speed high torque then decreasing the torque simultaneously as the speed is varying from high to low on each new torque step. The NRTC is a transient cycle with a collection of points for different torque and speed. The non-road emissions are also tested on the steady state cycle, C1, which is equivalent with the ISO 8178 cycle. The C1 cycle has total of 8 points with two different engine speeds varying the torque on 4 points on each speed level (Dieselnet, 2017).

4 Method

The project was divided into two separate parts, DOC and DPF. Each part sequentially represents a literature study, modeling and optimization in GT-SUITE and comparison to test cell data. The models were then joint together and evaluated using different sets of test cell data.

In the literature studies the chemical and physical phenomena occurring in the catalyst are studied. After the literature studies, the hard specifications of the system was noted from the Stage V HDEP-system. The test cell data was provided during the project after specific requests.

The specification of the system includes parameters such as materials, precious metal loadings, washcoat composition, pore sizes, cell densities and geometries of the substrate and filter. The parameters of interest from the test cell data were concentrations of CO, CO_2, HC, NO, NO_x, O_2 and soot. Mass flow rates and temperature were also retained, as well as pressures. The sensors for the measurements used to calibrate the DOC, were placed according to Figure (13) to capture the change in concentration and temperature over the DOC. The measurements used for the DPF model were taken according to Figure (14). The placement of the pressure sensors could not be changed and the sensors for temperature and concentration had three different positions possible before DOC, between DOC-DPF and after DPF.

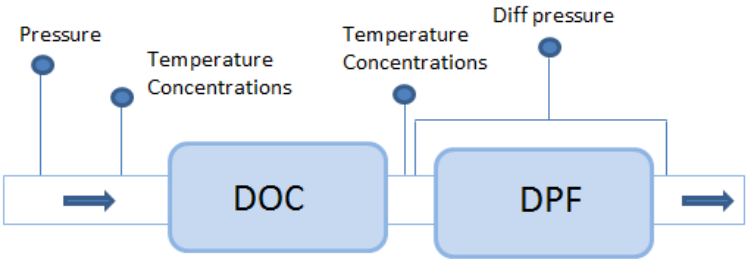

Figure 13: Measurement locations for modeling of DOC

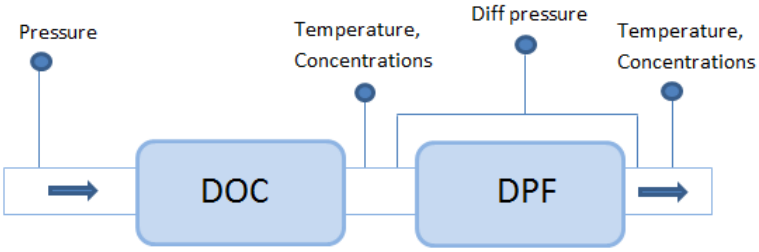

Figure 14: Measurement locations for modeling of DPF

When combining the DOC and the DPF models, inlet data where gathered according to Figure (15), that is no measurements were taken of temperature and composition between the DOC and DPF.

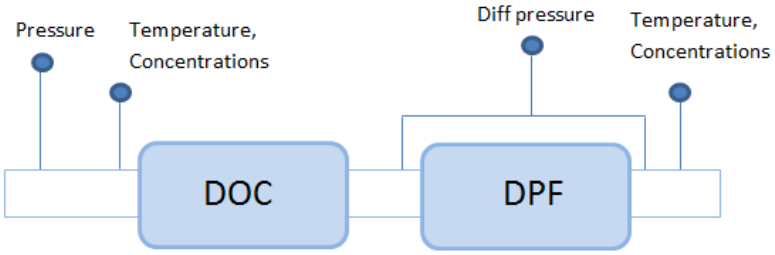

Figure 15: Measurment locations for modeling of DOC+DPF

The composition of HC was divided into three parts, fast oxidized propylene, the slow oxidized, but not adsorbed diesel fuel (gas) and the slow oxidized, diesel fuel, which was able to be adsorbed by the washcoat (gas+liquid) (Sampara et al., 2007). The initial ratio between them was assumed to be 50, 25, 25 % respectively, which is calculated from the inlet data according to Equations (34). However, that ratio was tested according to the four cases in Table (7).

$$[Propylene] = \frac{[HC] \cdot 0.5}{3} \qquad [Diesel\ fuel] = \frac{[HC] \cdot 0.25}{13.5} \tag{34}$$

Table 7: Four cases with different compositions of HC

Case	Propylene [%]	Diesel fuel, gas [%]	Diesel fuel, adsorbed [%]
1	50	25	25
2	40	30	30
3	30	35	35
4	20	40	40

The mole fraction of H_2 and H_2O was calculated according to Equations (35) based on recommendations made by Gamma technology, who based their assumption on the syngas reaction.

$$[H_2] = \frac{1}{3.5}[CO] \qquad [H_2O] = [CO_2] \tag{35}$$

The measured NO_x includes by default NO and NO_2, so NO_2 was calculated by subtracting NO from NO_x.

The models were tested and optimized against outlet test cell measurements. Table (8) describes the test plan about which data were used to optimize and validate the models. There was no validation of the DOC due to lack of test cell data different from PLM data. Both the DOC and DPF models were calibrated using the PLM data and the validations and evaluating of the models were based on transient cycles.

Table 8: Testplan for model and validation of DOC, DPF and DOC+DPF

Type	Model	Validation
DOC	PLM	-
DPF	PLM	NRTC
DOC+DPF	C1	NRTC

4.1 Connections and isulation

The pipe before DOC, between DOC and DPF and after DPF was modeled as being straight. The external convection temperature was assumed to 300 K and the external heat transfer coefficient, h, was adjusted to fit measured temperature. The material and insulation around the substrate and filter are described in Figure (16). The first layer was a supporting mat, assumed to be 6 mm thick with properties given by the supplier. The second layer was taken to be 1.5 mm thick steel shell, with properties of stainless steel stated in GT-SUITE library of materials. The third layer was air in between the shell around the substrate and filter against the muffler wall. This layer is uneven around the substrate and filter in reality but modeled as even. The air thickness layer was also optimized along h as the heat transfer rate parameters, to fit temperature data. To model the temperature the heat capacity could also be optimized, however, this was not done and the focus for temperature modeling were to vary the external heat transfer coefficient and the air thickness layer. The properties of the air were provided by GT-SUITE. The muffler wall consists of three layers, first a tin layer assumed to be 1.5 mm, then an insulation mat, 5 mm and finally another tin shell, 1.5 mm. The properties of tin was retrieved from engineeringtoolbox.com (Engineeringtoolbox, 2017) and the properties of the insulation mat was given by the supplier. The pipe and connections to the DOC and DPF had only the muffler wall as outer layer, thus tin, insulation and tin.

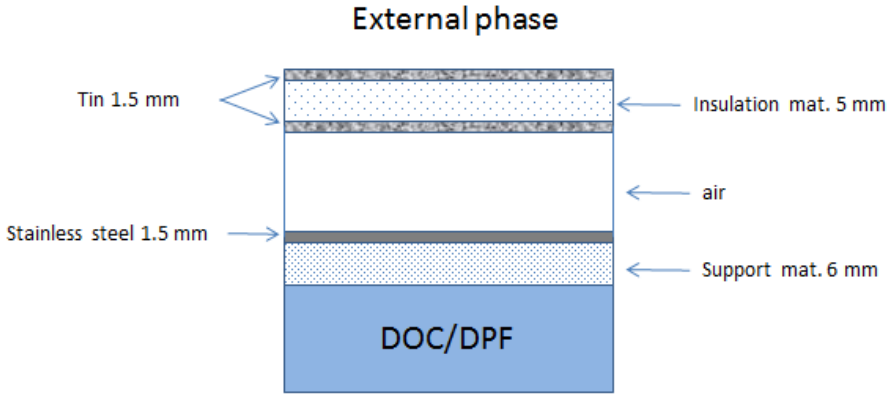

Figure 16: External layers of canning and insulation, where Substrate includes DOC and DPF

4.2 DOC

The DOC model includes specifications of the brick used and what inlet and boundary conditions the model used. The optimization method and what parameters that has been optimized in the DOC model is also found in this chapter.

4.2.1 Specifications

In GT-SUITE the DOC was modeled by a catalyst brick with connected reactions and an inlet- and outlet bricks seen in Figure (17). The inlet- and outlet pipes are built with cone bricks, where the inlet cone has an assumed cone angle of 7° and the outlet cone represents the straight pipe between the DOC and the DPF. The noncond parts on either side of the substrate seen in Figure (17), connects the pipes and the substrate brick without any heat loss. Since the pipe and the brick had the same diameter, there was no pressure loss in the connection. The chemical reactions were entered in the reaction brick and connected to the substrate via a connection used to plot reaction rates and other kinetics, Figure (17).

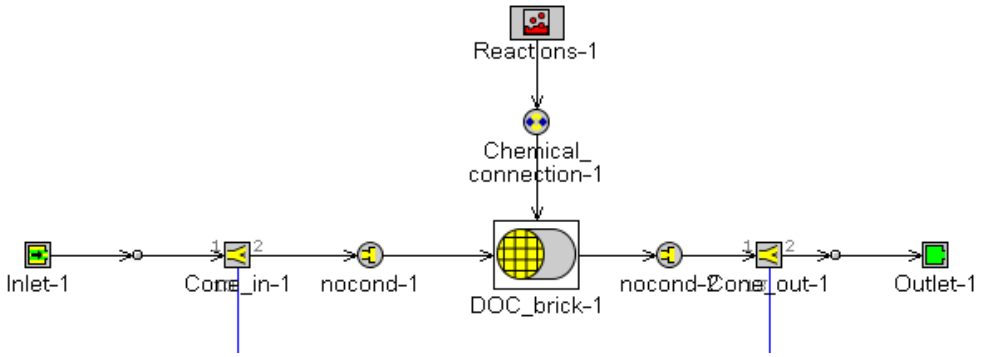

Figure 17: Model of DOC in GT−SUITE. The flow enters at Cone 1 and leaves at Cone out. The DOCbrick−1 is the substrate and the Reactions−1 includes all the kinetics

The substrate in the DOC was ceramic with a honeycomb structure which in the model was approximated with a square structure that assumed perfect packing. The geometric properties of the DOC can be seen in Figure (10).

4.2.2 Boundary & initial conditions

At the boundary of the substrate the wall temperature is calculated with a heat loss entry. The mass loss due to diffusion is assumed to be zero at the wall of the substrate. The initial condition entered in the model is assumed to be air at 1 bar and $500°C$.

4.2.3 Parameter Estimation

There are several parameters of interest to optimize in the DOC model. The goal was to tune the parameters to match the measured test cell data. The summarized squared error SSE, between the simulated results and the measured output from the model was calculated according to Equation (36), i.e. To account for differences in concentration between the species a weight function W, was used to decrease the tendencies for a biased optimization between the reactions when the differences for CO, HC and NO were summarized.

$$SSE = W\Sigma(measured - simulated)^2. \tag{36}$$

By optimizing the pre-exponent multiplier and the activation energies for Reaction (19) to (23) and minimizing $SSE_{CO,HC,NO}$, the parameters are tuned to match the real test cell data.

Figure (18) describes how the PLM cycle runs for the modeling of DOC. It starts at high torque and high speed and travels down in torque changing the speed from low to high in each change of torque. Finally it ends at low torque and high speed.

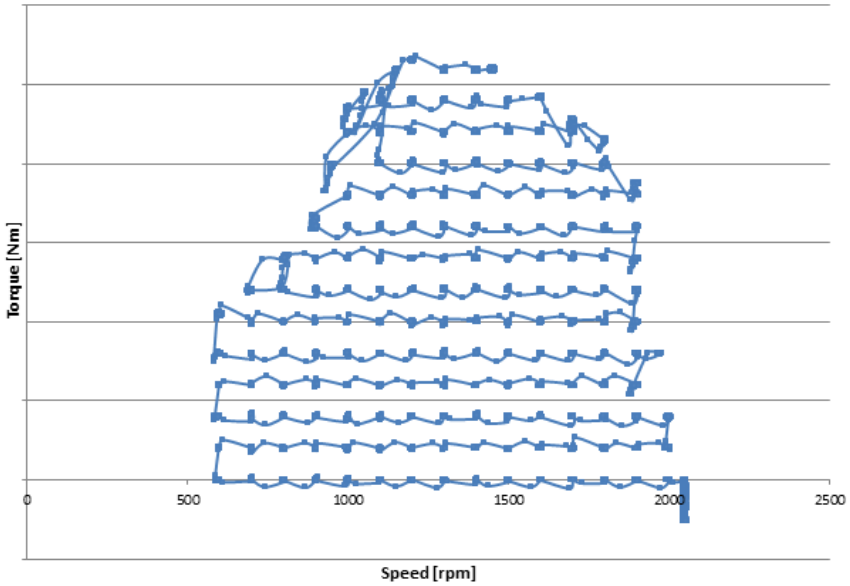

Figure 18: PLM cycle operating points used for DOC model

In Figure (19) the engine torque and speed is shown secretly versus the time for a PLM. Here the gradual decrease in engine torque is clear and also the periodic shift in engine speed over the cycle.

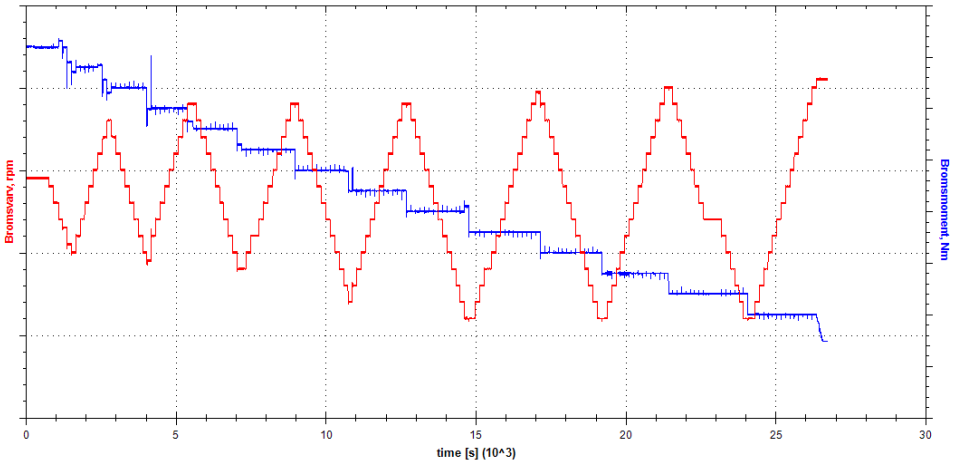

Figure 19: Speed rpm (red line Y1 axis) and torque Nm (blue line Y2 axis) versus time for the PLM cycle

The inlet is where the temperature, mass flow and composition from the engine were entered into the model. The mass flow and temperature profiles shown in Figures (20a) and (20b). The mass flow varies from 0.5-0.6 kg/s to about 0.1 kg/s in the same manner as the speed seen in Figure (18).

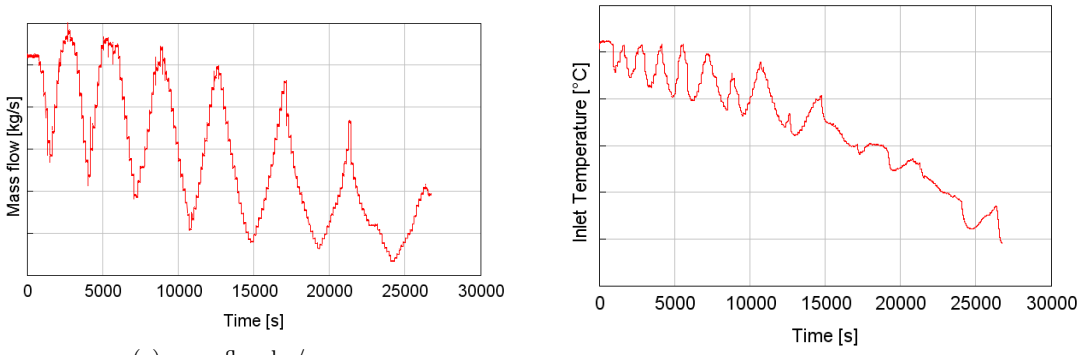

(a) mass flow kg/s

(b) Temperature °C

Figure 20: Inlet data for DOC model

The loading of the platinum metals in the washcoat and the atomic weight were known and according to Equation (13), the dispersion factor or the active site density is needed in order to calculate the other. In this model the dispersion factor was chosen to be optimized and the active site density was therefore calculated.

Activation energies and pre-exponent multipliers are tuned against the summation of the integrated errors for the oxidation reactions of CO, HC and NO. They were all optimized together, since they affect the temperature and thus each other's reactions. The algorithm used was the generic algorithm with population size 40 and number of generations 10.

The heat loss of the outer wall layer includes a heat transfer coefficient for the ambient air. This was also optimized to minimize the temperature difference between the measured values and the simulated results.

Table (9) describes the chosen parameters which where optimized, the reference objects that were minimized and the ranges in which the parameters values were allowed to vary. The table also includes the algorithm used for each optimization, provided by GT-SUITE. The dispersion factor was optimized first, then the activation energies, E_a and the pre-exponent multipliers, F, simultaneously, since they affect each other and last the external heat transfer coefficient, h together with the external air thickness layer. The exponential value of the pre-exponent multiplier was the parameter value that was optimized in order to weight the parameters moderately equally.

Table 9: Optimization parameters DOC

Optimized parameter	**Reference object**	**Lower limit**	**Higher limit**	**Algorithm**
Dispersion factor	SSE (CO, HC, NO)	5%	35%	Simplex
Ea_{CO} [J/mol]	SSE (CO, HC, NO)	$6{\cdot}10^4$	$10{\cdot}10^4$	Generic
F_{CO}	SSE (CO, HC, NO)	9	15	Generic
Ea_{NO} [J/mol]	SSE (CO, HC, NO)	3000	$10{\cdot}10^4$	Generic
F_{NO}	SSE (CO, HC, NO)	1	4	Generic
$Ea_{propylene}$ [J/mol]	SSE (CO, HC, NO)	$14{\cdot}10^4$	$19{\cdot}10^4$	Generic
$F_{propylene}$	SSE (CO, HC, NO)	16	21	Generic
$Ea_{dieselfuels}$ [J/mol]	SSE (CO, HC, NO)	$15{\cdot}10^3$	$32{\cdot}10^3$	Generic
$F_{dieselfuels}$	SSE (CO, HC, NO)	3	7	Generic
h [W/m^{2}K]	SSE (Temperature)	4	50	Simplex
Air thickness layer [m]	SSE (Temperature)	0.01	0.06	Simplex

4.3 DPF

The DPF model includes specifications for the filter and inlet and boundary conditions. The parameters selected and what methods used to optimize them are also stated in this section.

4.3.1 Specifications

The DPF was modeled with a filter brick connected to two reaction parts, one to the reactions regarding the cake layer of soot and one to the wall reactions of the channels. The filter was also connected to an inlet- and outlet cone, representing the pipes, as illustrated in Figure (21).

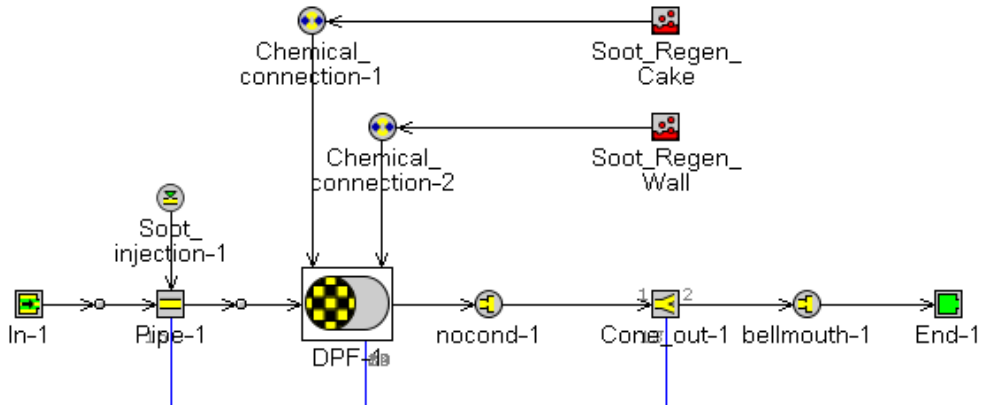

Figure 21: The GT-SUITE model of DPF. Soot injection and chemical reactions for regeneration and oxidation

The filter was constructed according to Figure (11a). The legth of the axial intervals were set to 30 mm, the clean filer permeability was calculated and the diffusion was activated.

The initial soot loading of the DPF was assumed 2 g/L. By calculating the volume of the DPF based on set geometry, the loading was 4.48 g in total. According to Figure (22) the total amount of initial soot load was divided solely on the wall layer, since the amount of soot and the pressure drop were so low. This total amount of initial soot load was miscalculated when converting the units, more about the consequences in Chapter 5.2.7.

4.3.2 Boundary & initial conditions

The boundary conditions for the DPF is the inlet temperature, mass flow and concentration of CO, HC, NO, H_2, H_2O, N_2, O_2 and soot. The initial state in the DPF consist of air of 509 K based on the measured value at t = 0 and initial assumed pressure of 200 kPa. The filter used has an unknown initial soot loading. The initial soot is guessed by the user and the division between the soot cake and the wall for this initial soot is done according to Figure (22). Where the total initial soot loading, blue line, is the summation of the soot in the cake layer, green line, and the wall, pink line.

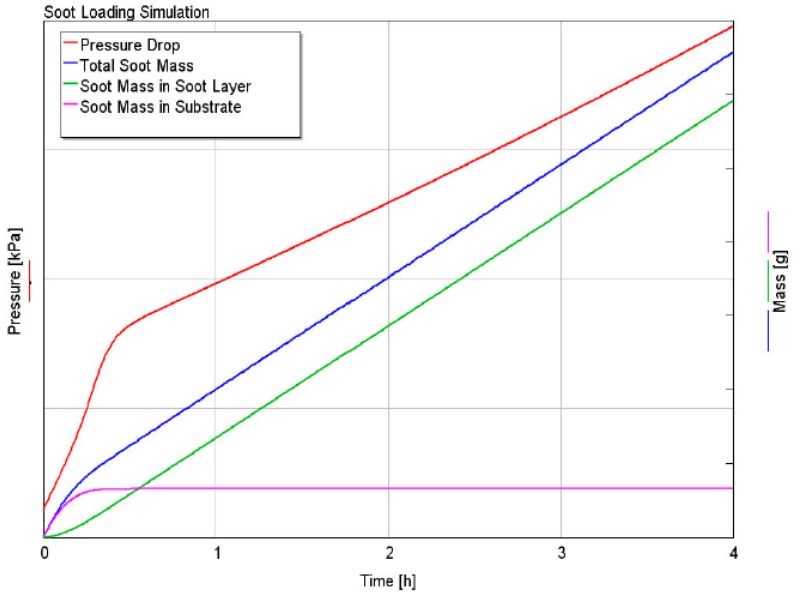

Figure 22: Initial soot loading division

4.3.3 Parameter Estimation

The DPF was modeled using a PLM cycle with speed-torque shown in Figure (23).

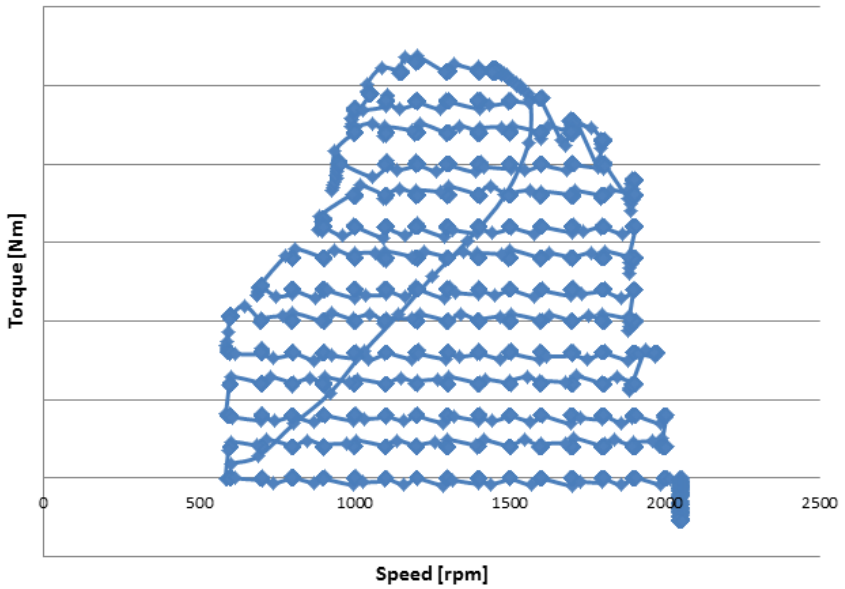

Figure 23: PLM cycle operating points used for DPF model.

The inlet mass flow and the temperature to the DPF model are illustrated in Figures (24a) and (24b). The mass flow varies from 0.6 kg/s down to about 0.1 kg/s. The temperature starts high at 500°C and varies down to about 100 °C. These trends are based on differences in torque and speed. High torque and high speed corresponds to high mass flow and high temperature.

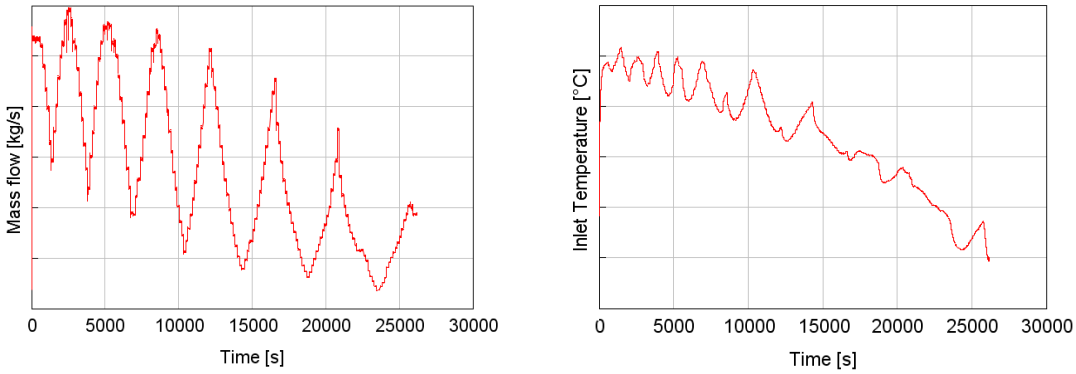

(a) Mass flow kg/s

(b) Temperature °C

Figure 24: Inlet data for the DPF model

Since the DPF was also coated with precious metals the oxidation reactions of CO, HC and NO was too optimized. The parameter ranges used can be seen in Table (10). The reason for not using the same parameter ranges as for the DOC optimization was that there is no soot oxidation in the DOC and the structure of the brick is different resulting in changed parameter ranges. In fact since all the parameters have been tuned based on measurements, means that the models are only valid for those specific conditions. Since all the activation energies and pre-exponent multipliers are optimized simultaneously, the generic algorithm was used. When optimizing the external heat transfer coefficient and the air thickness layer the simplex algorithm was used since there were only two parameters. Simplex was also used when optimizing the initial soot loading for the same reason.

Table 10: Optimization parameters DPF

Optimized parameter	**Reference object**	**Lower limit**	**Higher limit**	**Algorithm**
Ea_{CO} [J/mol]	SSE (CO, HC, NO)	$6{\cdot}10^4$	$1{\cdot}10^5$	Generic
F_{CO}	SSE (CO, HC, NO)	8	14	Generic
Ea_{NO} [J/mol]	SSE (CO, HC, NO)	1500	10 000	Generic
F_{NO}	SSE (CO, HC, NO)	1	4	Generic
$Ea_{propylene}$ [J/mol]	SSE (CO, HC, NO)	$14{\cdot}10^4$	$19{\cdot}10^4$	Generic
$F_{propylene}$	SSE (CO, HC, NO)	16	21	Generic
$Ea_{dieselfuels}$ [J/mol]	SSE (CO, HC, NO)	$15{\cdot}10^3$	$32{\cdot}10^3$	Generic
$F_{dieselfuels}$	SSE (CO, HC, NO)	3	7	Generic
h $[W/m^2K]$	SSE (Temperature)	10	50	Simplex
air thickness layer [m]	SSE (Temperature)	0.01	0.06	Simplex
Initial soot loading, wall [g]	SSE (Pressure drop)	0	10	Simplex
Initial soot loading, cake layer [g]	SSE (Pressure drop)	0	10	Simplex

4.3.4 Validation

In order to validate the DPF model, data from the non-road transient cycle NRTC, were used. The NRTC speed-torque operating points are shown in Figure (25).

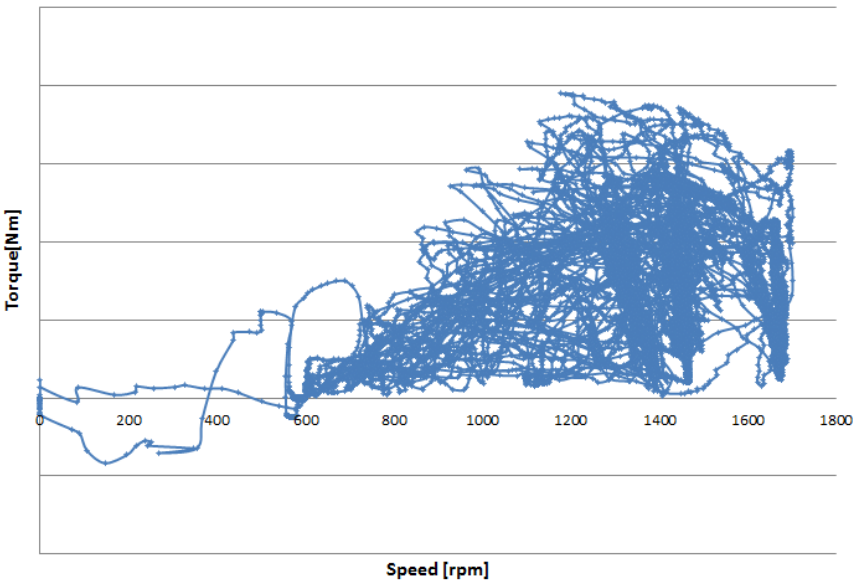

Figure 25: NRTC operating points

The initial mass flow and temperature into the DPF are presented in Figures (26a) and (26b).

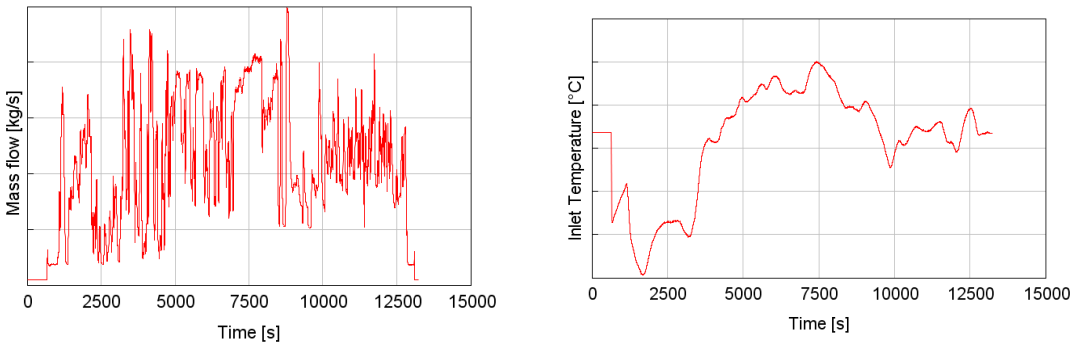

(a) Mass flow kg/s

(b) Temperature °C

Figure 26: Inlet data for DPF validation

4.4 DOC+DPF

The optimized model for the DOC was coupled with the optimized model for the DPF. The combined model was tested for both a C1 and NRTC cycles. The injection of the soot, which actually comes from the engine, was moved to the cone before the DOC in order to get the right injection temperature.

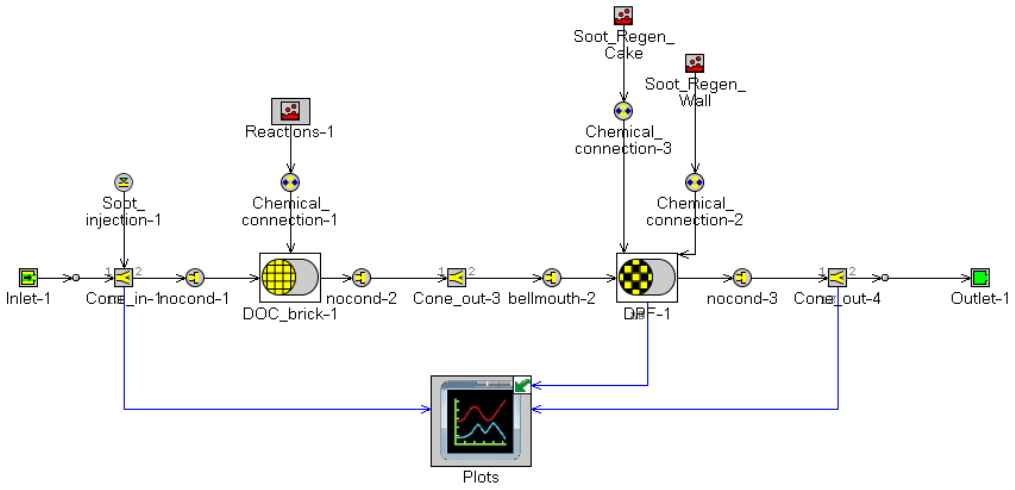

Figure 27: Schematic figure over the combined model for DOC+DPF

4.4.1 C1 cycle

The combined DOC and DPF model was run using the C1 cycle described in section (3.5) , with torque and speed points according to Figure (28). The inlet temperature and mass flow are presented in Figures (29a) and (29b).

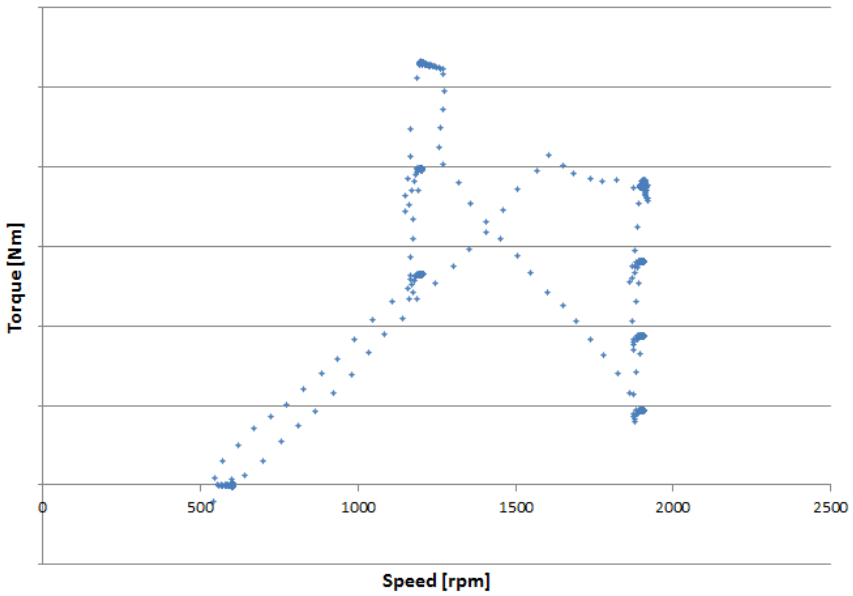

Figure 28: C1 cycle operating points

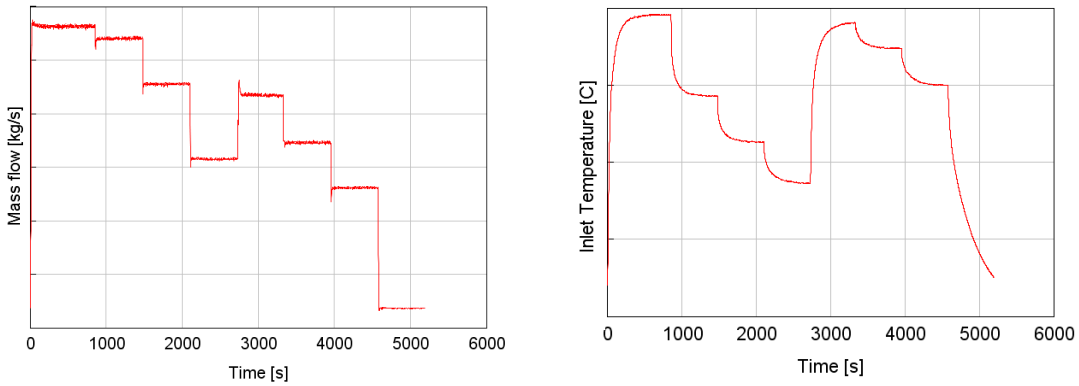

(a) Mass flow kg/s

(b) Temperature °C

Figure 29: Inlet data for DOC+DPF model with C1 cycle

4.4.2 NRTC

To validate the combined DOC–DPF model the NRTC was used as well in order to capture any errors the C1 cycle did not. The operating points for the NRTC are illustrated in Figure (25). The Inlet mass flow and inlet temperature are presented in Figures (30a) and (30b).

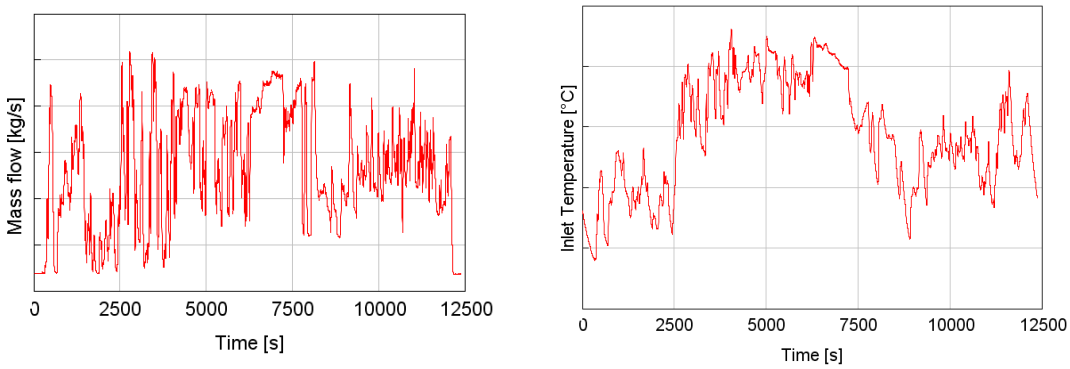

(a) Mass flow kg/s

(b) Temperature °C

Figure 30: Inlet data for the DOC+DPF model with NRTC cycle

5 Results

5.1 DOC

When changing the composition for HC according to Table (7), case 2 with 40% propylene gave the most accurate result when comparing simulated HC concentration against the measured HC values out of the DOC. Since propylene has a higher activation energy it needs more energy to oxidize. To decrease the simulated result at the low temperature region of the cycle, the amount of propylene was lowered to match the measured values. In order to be able to couple the DOC model to the DPF model, the case 2 composition of HC was also used in the DPF simulation.

5.1.1 Dispersion Factor

The result for the optimization of the dispersion factor DF, in the washcoat layer against the summation of error between measured concentrations and simulated result $SSE_{CO,NO,HC}$, is presented in Figure (31). The optimization parameters are summarized in Table (9) were the limits were recommended by Gamma Technologies based on their previous experiments and knowledge. As seen in Figure (31), a lower value of the dispersion factor is favorable in order to get the lowest error between simulated and measured values of concentrations. Noticeable is the outliner at a dispersion factor of 0.0725, this point is however, not relevant since the dispersion factor converges at 0.0575.

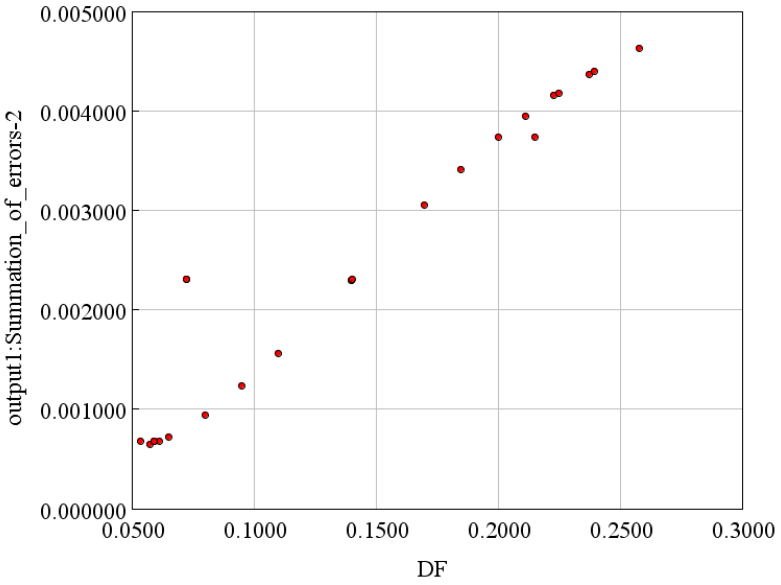

Figure 31: The result from optimization of dispersion factor, DF versus $SSE_{CO,NO_x,HC}$

5.1.2 External Heat Transfer Coefficient and Air-thickness Layer

The results from optimization of the external heat transfer coefficient can be seen in Figure (32). The reference object was the summarized squared error between the simulated and measured temperature out from the DOC. The results indicate an optimized value of 7.2 W/m^{2}K. Figure (33) illustrates the optimization of the air-thickness layer which gives the result of 0.012m. Comparing Figures (32) and (33) it is noticed that h has a greater effect on $SSE_{Temperature}$ then the thickness

of the air layer. Almost the entire range of the thickness gave similar result for the error compared to the heat transfer coefficient which converged at 7.2 W/m^{2}K. Thus there is a large heat gradient between the external surface and the surroundings compared to between the brick and the external surface, resulting in h having a larger impact on the error in temperature simulation.

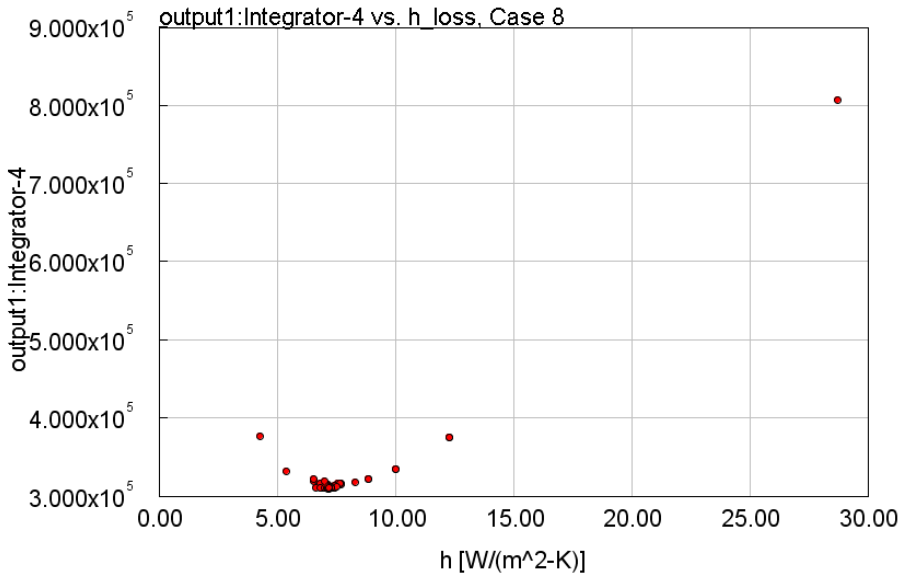

Figure 32: The result for optimized external heat transfer coefficient h versus integrated $SSE_{Temperature}$

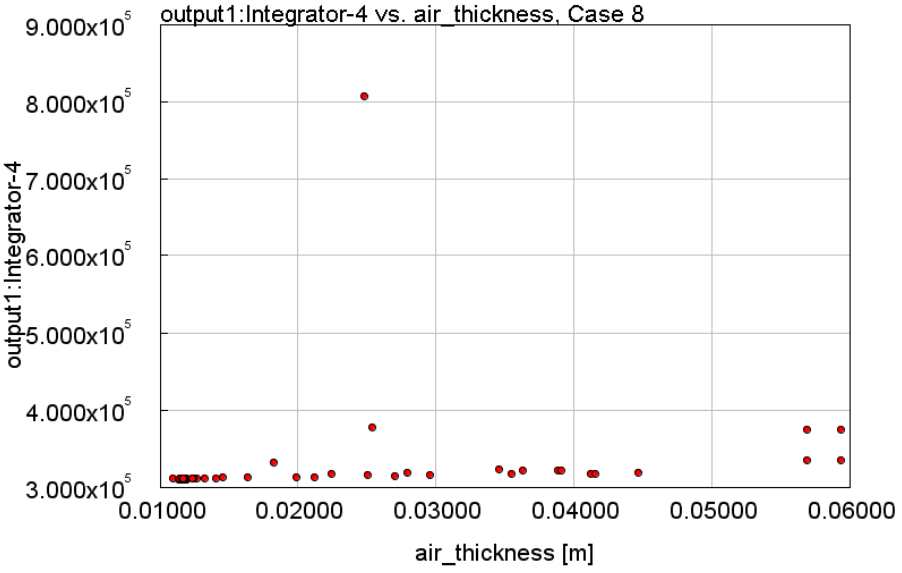

Figure 33: The result for optimized air-thickness layer versus integrated $SSE_{Temperature}$

With the optimized parameters for Ea, F, h and the air-thickness were used to simulated the following Figures. Figure (34) shows the results for simulated and measured outlet temperature versus time. To illustrate that there is not a big change in temperature between the DOC inlet and DOC outlet, the inlet temperature is also plotted in Figure (34). Figure (35) plots the error in % between the simulated temperature and the measured temperature on the Y1 axis and the

actual difference on the Y2 axis. There are three bigger peaks, indicating shortcomings of the model, with the highest deviation from measured values of about 5%, which is not high, but the actual difference shown with the blue line, is about $20°C$ at those points which is a remarkable difference. The three points are at about 15000 s, 19000 s and 24000 s and represents low speed points were the torque shifts down, Figure (18). Consequently the model has difficulties to capture the accurate temperature during low speed when the torque shifts to a lower value.

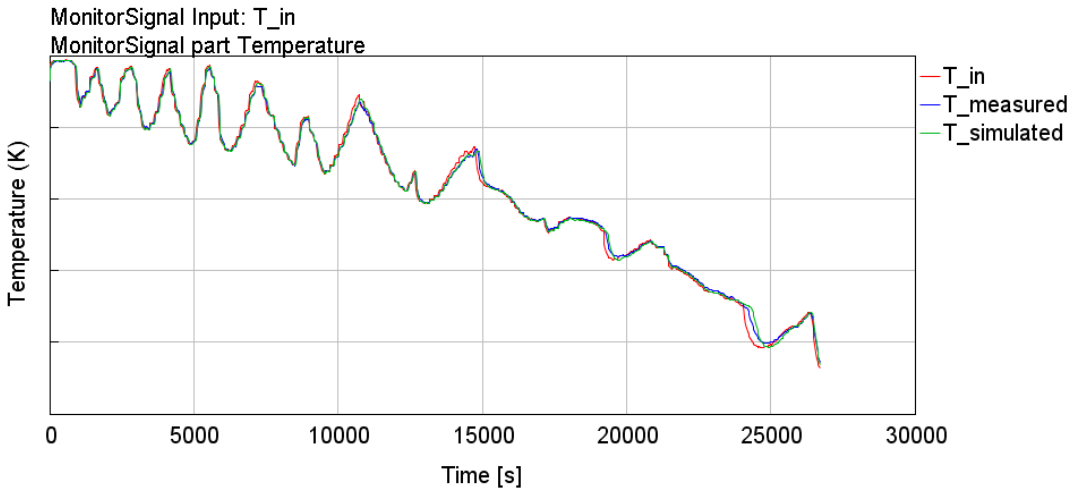

Figure 34: Result of simulated temperature versus time with inlet temperature and measured outlet temperature for DOC model.

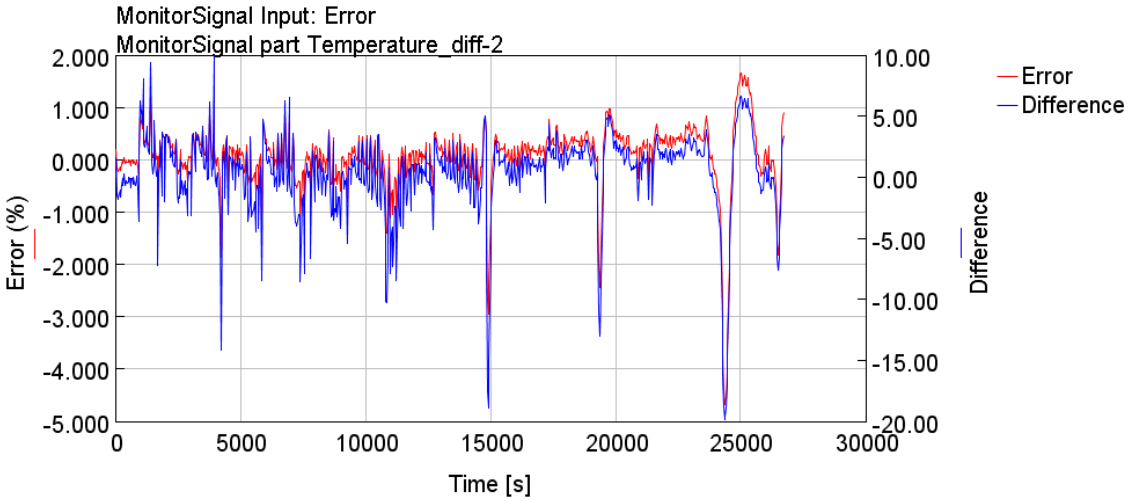

Figure 35: Result of error between simulated- and measured temperature for DOC model

Since the reactions are exothermic, heat will be produced. To get a better fit for the temperature over the DOC the external heat transfer coefficient could be optimized along with the heat capacity of the different species. In this project, the heat capacities were determined by the software and thus an optimization of them were outside the scope of the project. Optimizing more parameters influencing the temperature, would probably give better results.

5.1.3 Activation Energies and Pre-exponent Multipliers

The results from the optimization of activation energies and pre-exponent multipliers are presented in Table (11). As mentioned previously in Section (6), it was the exponent of the pre-exponent multiplier that was varied. For example, the result for the optimization of F_{CO} was $10^{12.03}$ were the optimized value was 12.03. The calculated reaction rate constant for each species, calculated using Equation (12), at the temperature of 373 K is also shown in Table (11).

Table 11: The optimized results for the activation energies E_a and pre-exponent multipliers F for the oxidation of CO, NO and HC (propylene and diesel fuel)

Substance	E_a [J/mol]	F	T [K]	k_m
CO	91598	$10^{12.03} \simeq 1.07 \cdot 10^{12}$	373	0.16
NO	3135	$10^{2.41} \simeq 257$	373	93.52
$Propylene$	142509	$10^{20.58} \simeq 3.8 \cdot 10^{20}$	373	4.20
$Dieselfuel$	29423	$10^{5.19} \simeq 155 \cdot 10^{3}$	373	11.75

Comparing the results in Table (11) to the results of E_a and F according to findings by Lundberg ((Lundberg et al., 2016)) presented in Table (12), it is the activation energy for CO that is similar between Lundbergs and the results from this thesis. The other parameter values differ significantly. Nevertheless comparing to the results from Voltz (Voltz et al., 1973) the E_a are also different to both Lundberg and the results in Table (11). Consequently the results presented by this thesis are not inaccurate just because it differs from literature values, since most papers presents different values themselves. The reaction rate constant for each species at 373K was also calculated based on Lunbergs findings in Table (12). When comparing the values of the rate constants in Table (11) to those in Table (12), a large difference between the results for NO concentration is observed. Even though F_{NO} is larger in Lundbergs than in this projects it results in a smaller rate constant indicating the large impact the activation energy has on the reaction rate expression.

Table 12: The result for E_a and F according to (Lundberg et al., 2016)

Substance	E_a [J/mol]	F	T [K]	k_m
CO	99100	$2.05 \cdot 10^{14}$	373	2.72
NO	33900	$1.7 \cdot 10^{5}$	373	3.04

5.1.4 CO

In Figure (36) the mole fraction of CO versus time can be seen including the inlet, simulated and measured values. Comparing the simulated values green line, to the measured values blue line, the difference at the end of the cycle is large indicating an adjustment of activation energy and pre-exponent multiplier is necessary. Looking at Figure (36) after 5000 s, the inlet concentration and the measured values increase. Studying Figure (20a) the mass flow also increases at that time and in Figure (19) the speed is high and a shift in torque is seen. At 5400 s the inlet concentration increases again but the measured values does not and looking at the mass flow in Figure (20a) it decreases at about 5400 s. Again studying the speed at that point in Figure (19) it is low and the torque is shifting. At high torque and high and low speed the combustion is incomplete, whereas if the speed is at a medium level at high torque the combustion is closer to the optimum.

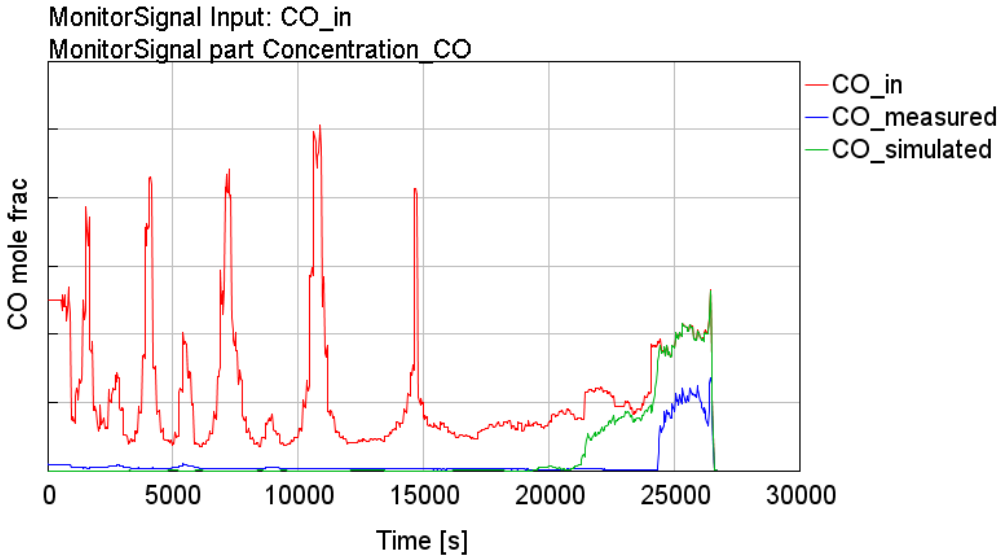

Figure 36: Result of Simulated CO concentration versus time for DOC model with inlet and measured outlet concentrations.

In Figure (37) the E_a and F have been manually changed to better fit the measured values at the low temperature and mass flow region. Ea_{CO} was changed from 91598 J/mol to 83000 J/mol and the exponent in F_{CO} was changed from 12.03 to 13. These values were iterated to get a better fit for the low temperature region of the cycle.

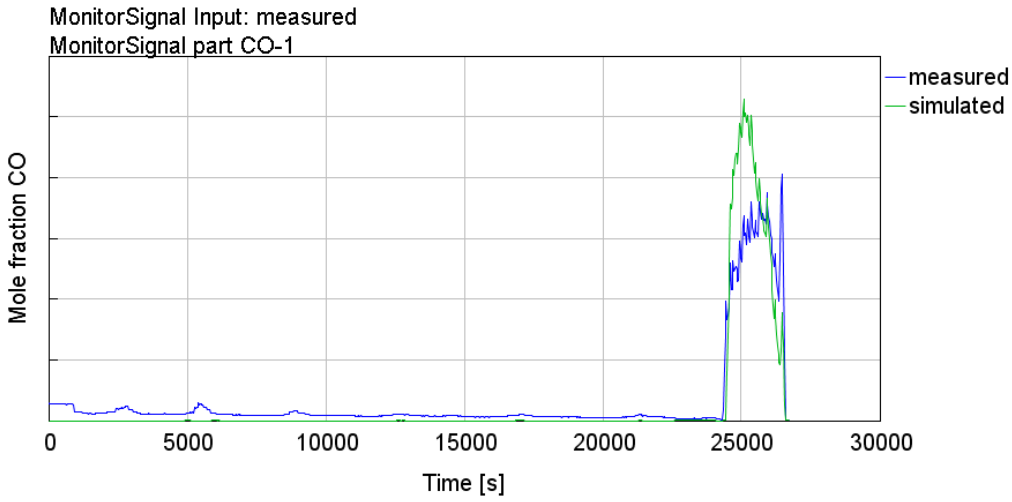

Figure 37: Results of simulated CO concentration versus time with changed activation energy and pre-exponent multiplier for DOC model, with measured CO concentration

When studying the measured values of CO in Figure (37) at high temperatures (beginning of the cycle) the conversion should be 100%, since the temperature is high, but there is a CO slip which the simulated results do not capture. Figure (38) illustrates the simulated CO conversion against inlet temperature and as mentioned, the conversion is about 100 % at temperatures above 450K (177 °C). Studying a CFD simulation over the DOC inlet velocity, Figure (39), a velocity gradient in the distribution over the substrate is clearly visible. This gradient will give varying values of Reynolds number in different channels of the DOC, affecting the Sherwood number and the mass

transfer coefficient. This non-uniform velocity into the DOC could also affect the temperature, resulting in a gradient between channels. The temperature affects the kinetics of the model and the channels with lower temperature would then result in lower conversion as seen in Figure (38). This could be the explanation to the CO slip in the high temperature region for the measured values. When optimizing Ea_{CO} and F_{CO}, every point in the cycle were included to lower $SSE_{CO,HC,NO}$. This means that the optimization algorithm were trying to increase the simulated CO at high temperature due to the CO slip in measured values, which resulted in a too high value for Ea_{CO} and F_{CO} at lower temperatures. An optimization based on the values in the lower mass flow and temperature region would probably result in a better fit of the kinetic parameters for CO oxidation.

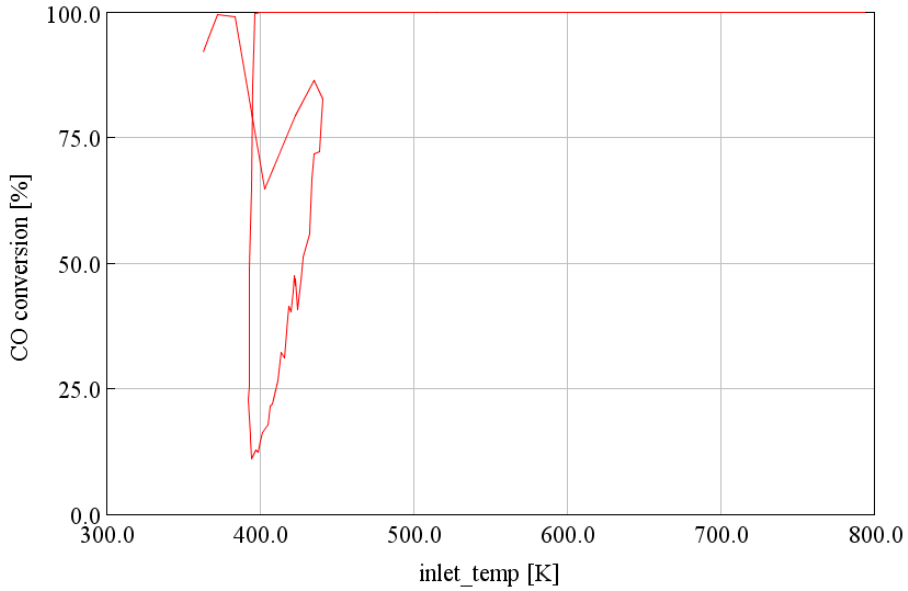

Figure 38: Simulated conversion of CO versus inlet temperature

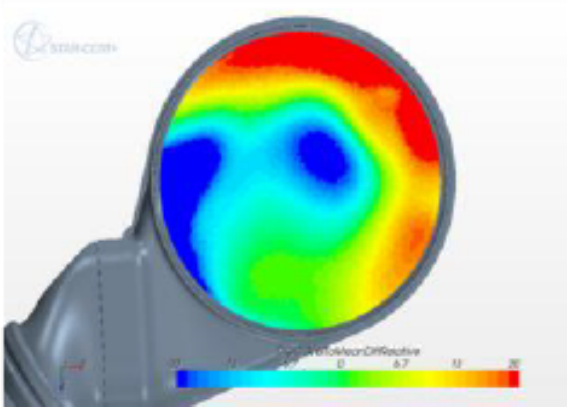

Figure 39: CFD simulation over inlet velocity to DOC. Blue indicates -20% of average velocity and red indicates +20% of average velocity.

The following figures for the DOC model are based on the change of Ea_{CO} and F_{CO} but when comparing with the original values there were next to no change in HC and NO concentration, so the manually iterated values for CO were used onwards. In Figure (40) the deviation of the simulated result to the measured values in %, red line, can be seen on the Y1 axis. While at the Y2 axis, the actual difference between the simulated result and measured values are plotted, blue line. In the high temperature region, the error is about 99% which is due to the CO slip. When the

conversion decreases further at the end on the cycle the difference decrease. However, the actual difference at the end of the cycle varies still from about -50 to 50 ppm.

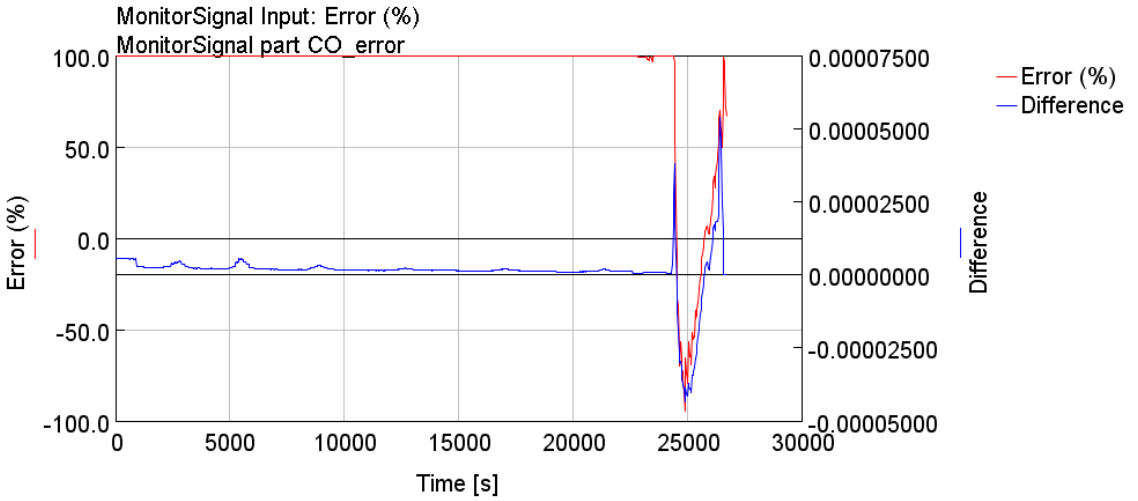

Figure 40: Result of calculated error between measured- and simulated CO concentration for DOC model

5.1.5 HC

The result for the HC concentrations can be studied in Figure (41) where the simulated-, measured- and inlet values are plotted versus time. The calculated error between the measured values and the simulated results for HC can be seen in Figure (42). The simulated result in % of measured values are plotted on the Y1-axis and the actual difference is plotted on the Y2-axis. Noticeable in Figure (41) is the large error between 19000 s to 24000 s, were the simulated result is higher than the measured values, probably compensating for the lower result in the beginning of the cycle, as for the CO simulation. Comparing the simulated trend of HC against the inlet mass flow Figure (20a), HC increases at mass flow peaks while the measured HC does not follow the varying pattern with the same magnitude. An explanation could be that the heat- and mass transfer resistance, assumed to be a set value by Nu and Sh, is not correct. Changing the Sh number would change the mass transfer coefficient according to Equation (9) and therefore change the mass transfer resistance. Another reason could be sampling issues were the measurement of HC is delayed and shows more smoothening effects, however this needs further investigations about the sensors used, and not included in this thesis.

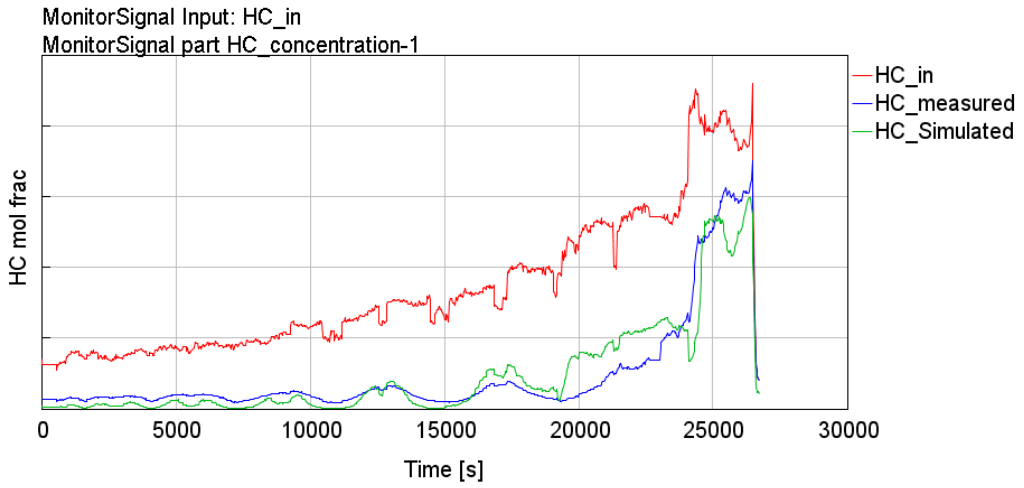

Figure 41: Result of simulated HC concentration against time, with inlet HC concentration and measured outlet values for DOC model

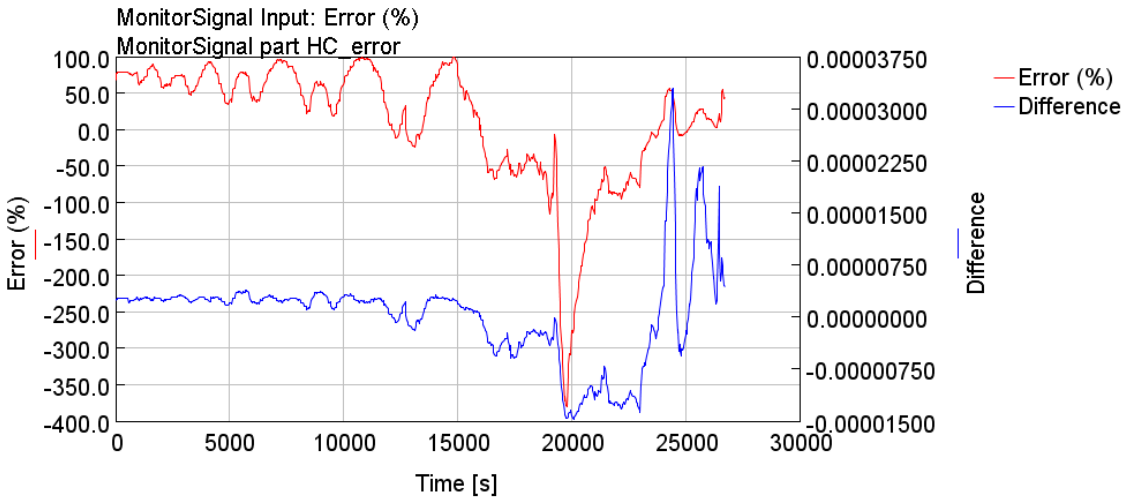

Figure 42: Calculated error between simulated and measured HC concentration for DOC model

5.1.6 NO

In Figure (43) the simulated result of NO concentration is plotted versus time, along inlet concentration and measured outlet values. Studying the end of Figure (43) at about 25000 s the measured NO values are higher than both the inlet concentration and the simulated outlet result, thus NO is being formed. This could be explained by Reactions (37) and (38) were NO_2 is used as an oxidation agent and NO is formed. Nevertheless, these reactions were not included in the model, but could have explained the error in the lowest temperature region where these reactions would be active.

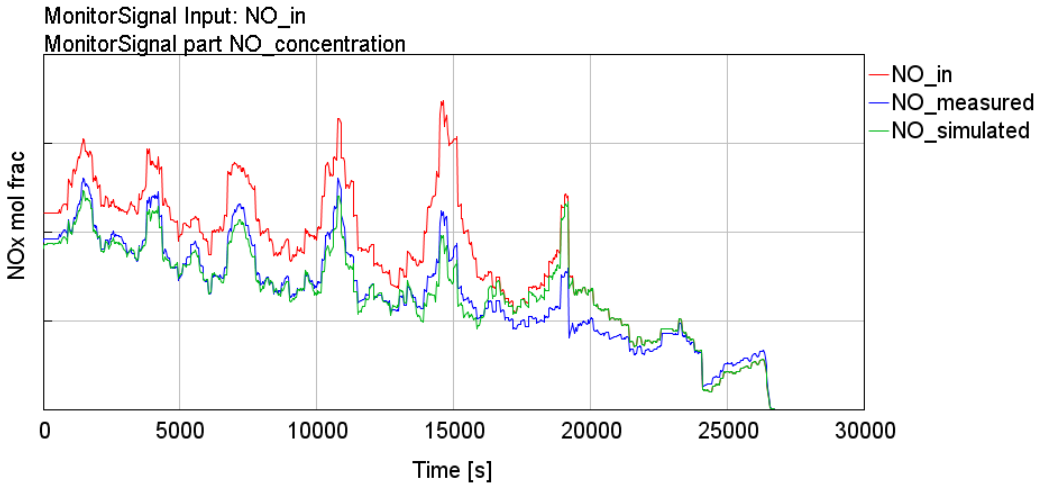

Figure 43: Result of simulated NO concentration against time with inlet and measured outlet NO concentration for DOC model

$$CO + NO_2 \rightarrow CO_2 + NO \tag{37}$$

$$2HC + 5NO_2 \rightarrow H_2O + 2CO_2 + 5NO \tag{38}$$

Figure (44) shows the deviation of simulated NO result to measured values in %. The error is around +/-5% during the first part of the cycle, however when the temperature decreases the NO-error increase before the conversion subsides and the error decreases again. It is at around 19000 s that the error is at the maximum value which also can be seen in Figure (43). Studying the peak values in Figure (43) at about 4000 s and 5500 s the simulated result is lower than the measured value. At 19000 s the simulated result is higher than the measured value resulting in the high error at that point. Since Ea_{NO} and F_{NO} are optimized based on the entire cycle, the optimization algorithm is trying to increase the simulated result for NO due to the difference at 4000 s and 5500 s. This could explain the higher values at 19000 s. An optimization based only on the lower temperature would probably result in a better fit for the kinetic parameters for NO.

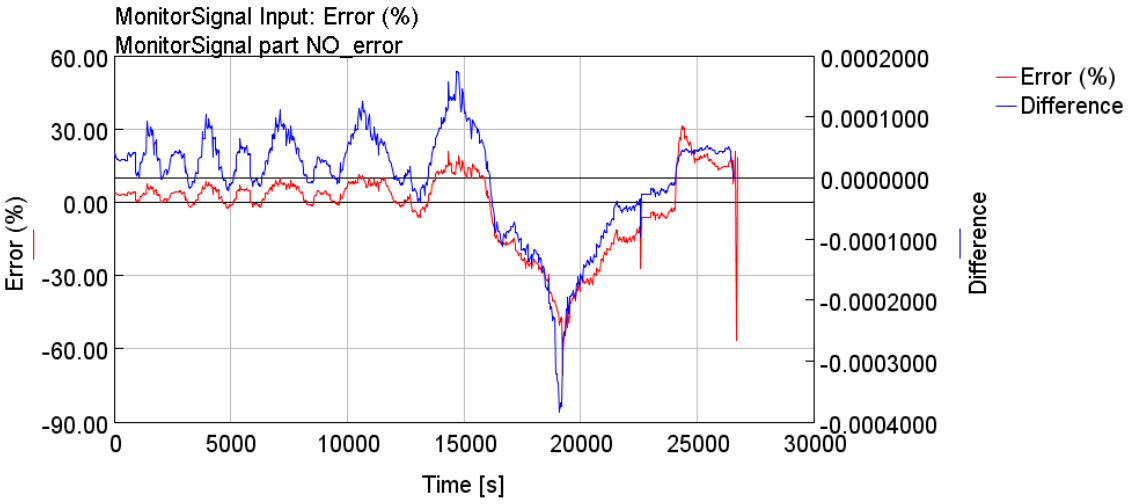

Figure 44: Calculated error between simulated and measured NO concentration for DOC model

Figure (45) shows the result for simulated NO conversion against inlet temperature. A peak in conversion can be seen between 600-680 K (327- 407°C) however, according to Lundberg (Lundberg et al., 2016) does the equilibrium maximum take place at 683-713 K and it is in this region the validation of the model should be done. Comparing the peak error in Figure (44) and the corresponding point in Figure (43) the conversion is almost zero since the simulated result almost follows the inlet concentration. Looking at Figure (45), the conversion is low at a temperatures below about 510 K (237°C), compared to literature value were the conversion subsides at about 200°C (Lundberg et al., 2016). An optimization of Ea_{NO} and F_{NO} at different temperature intervals would probably produce more accurate results, but this was outside the scope of this thesis.

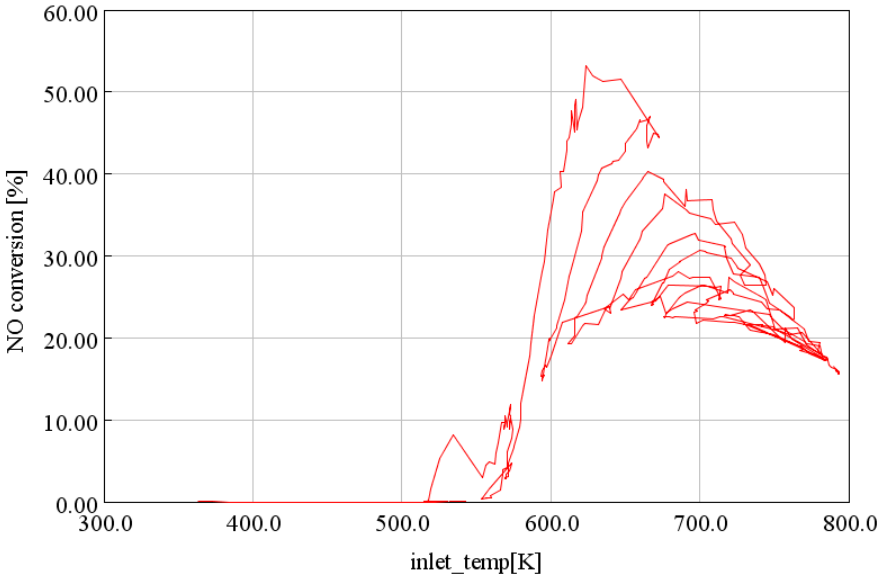

Figure 45: Simulated NO conversion versus inlet temperature

5.1.7 Conversion

The simulated conversion of the CO-, HC- and NO oxidation versus time can be seen in Figure (46), with the inlet temperature on the Y2 axis. It is noticed that NO-oxidation barely reaches above 50% conversion before dropping down again. Also interesting is how the HC conversion follows the trend of the inlet temperature, indicating that the conversion follows the temperature which is governed by the activation energy of HC.

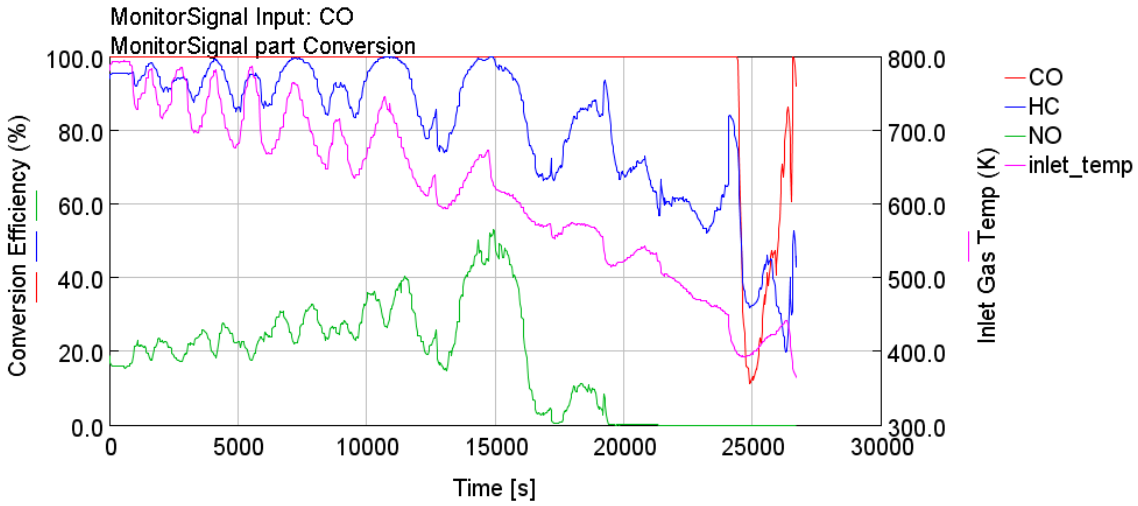

Figure 46: Conversion efficiency for CO, HC and NO against time on Y1-axis and Inlet temperature against time on Y2-axis

5.2 DPF

The DPF model was calibrated using a PLM cycle and validated using an NRTC.

5.2.1 External Heat Transfer Coefficient and Air-Thickness Layer

The optimization result for the external heat transfer coefficient did not converge at a lower limit of 5 W/m^{2}K. When comparing temperature results of h equal to 5 W/m^{2}K and 1 W/m^{2}sK, the later gave lower differences between simulated- and measured temperature. The value of 1 W/m^{2}K is probably not a reasonable value since it indicates an almost adiabatic reactor, but this is a simple model so 1 W/m^{2}K is used onward. The difference between 5 W/m^{2}K and 1 W/m^{2}K of simulated- and measured temperature is presented in Figures (47) and (48). An improvement of the simulated temperature can be seen at approximately 14000 s were the simulated temperature is higher (green line), than the measured value (blue line), in Figure (47). It follows the measured value better in Figure (48). The deviation from measured value in % for the simulated temperature is seen for an h-value of 5 W/m^{2}K in Figure (49) and for h equal to 1 W/m^{2}K in Figure (50). The actual difference between the simulated and measured temperature is plotted in the same figures as the blue lines. The improvement of lowering the external heat transfer coefficient can be seen more clear by comparing the error in % in Figure (49) and Figure (50). A higher external heat transfer coefficient seems to have an offset on the red line to 1 % error while in Figure (50) the red line is mainly varied arount 0 % error.

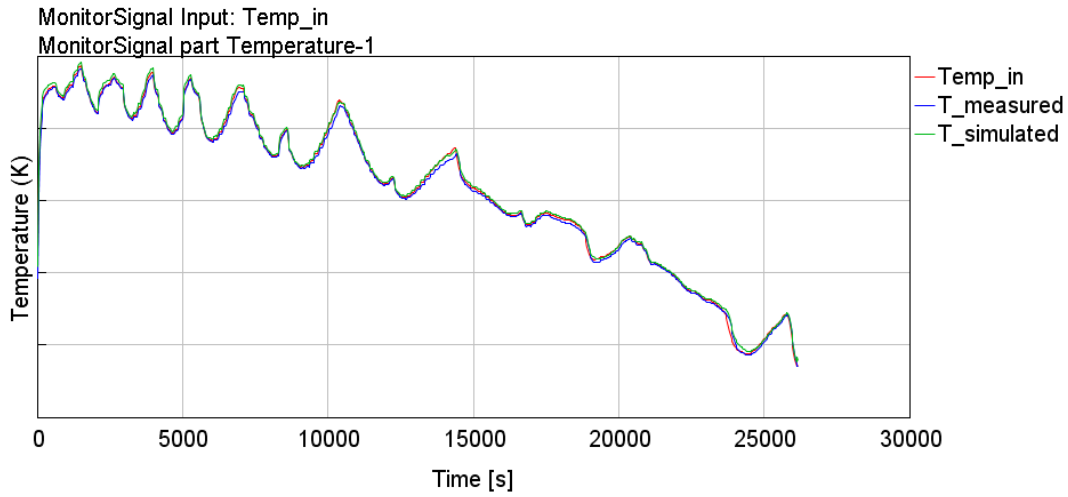

Figure 47: Result of simulated temperature versus time in DPF, with inlet- and measured temperature. For an external heat transfer coefficient of 5 W/m^2K

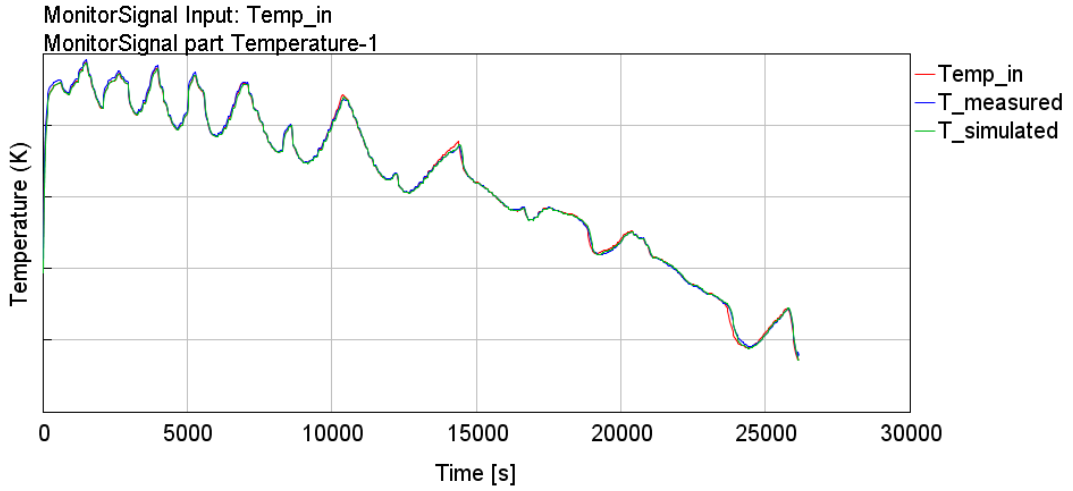

Figure 48: Result of simulated temperature versus time in DPF, with inlet- and measured temperature. For an external heat transfer coefficient of 1 W/m^2K

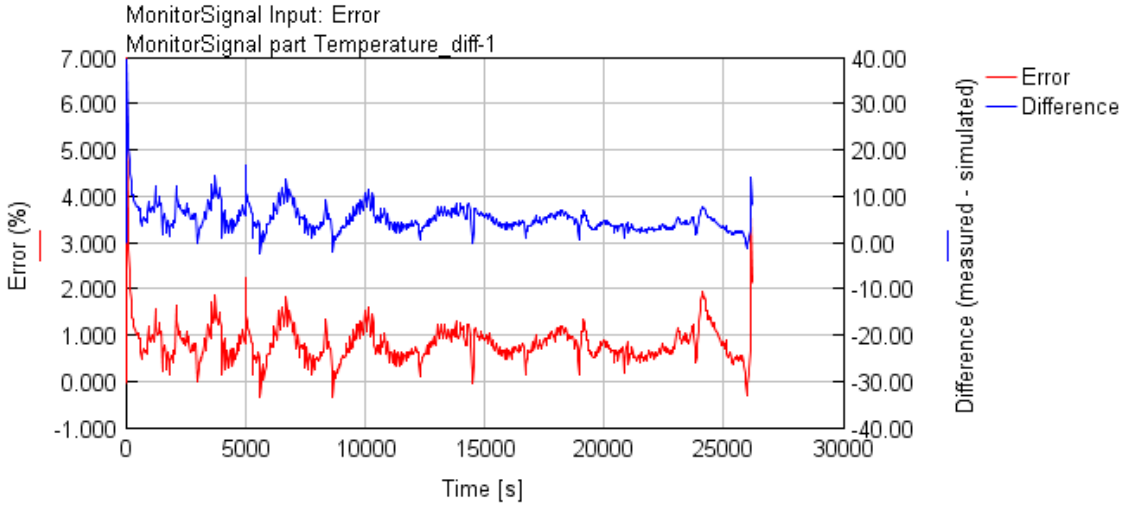

Figure 49: Calculated error between simulated and measured outlet temperature for the DPF model with h equal to 5 W/m^{2}K

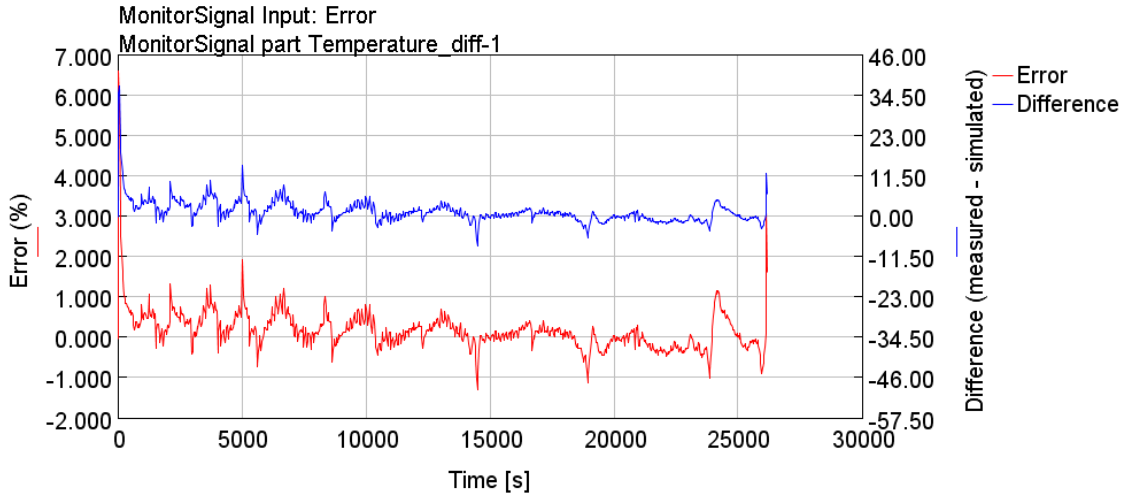

Figure 50: Calculated error between simulated and measured outlet temperature for the DPF model with h equal to 1 W/m^{2}K

As seen in Figure (50) it is in the beginning of the cycle were the largest error occur. Zooming in on the first 200 s of the cycle for the temperature, Figure (51) is formed. The simulated result seem to decrease first creating a large error to the measured values, which only decreases a little. Looking at the inlet data before simulation Figure (52), the outlet measurements blue line, has a smooth decrease in temperature before increasing along the inlet temperature red line, trend. The decrease in temperature can be due to previous cycles run on the system and since the mass flow green line, increases very fast the temperature would also increase. Consequently the simulated temperature does not change as quickly in the beginning as the measured values does. This should not be a problem if the measured data did not include this phenomenon.

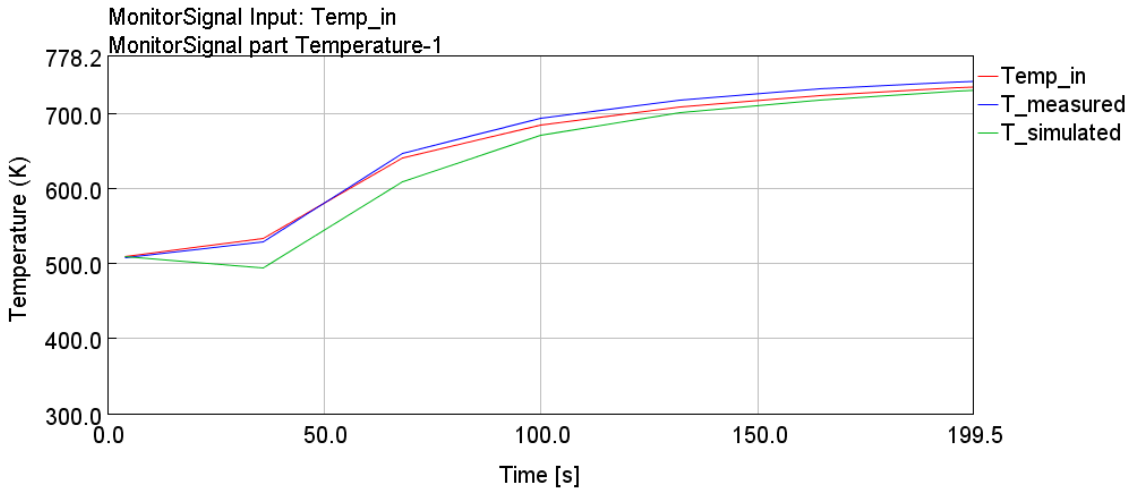

Figure 51: Zoomed image over simulated temperature of the DPF

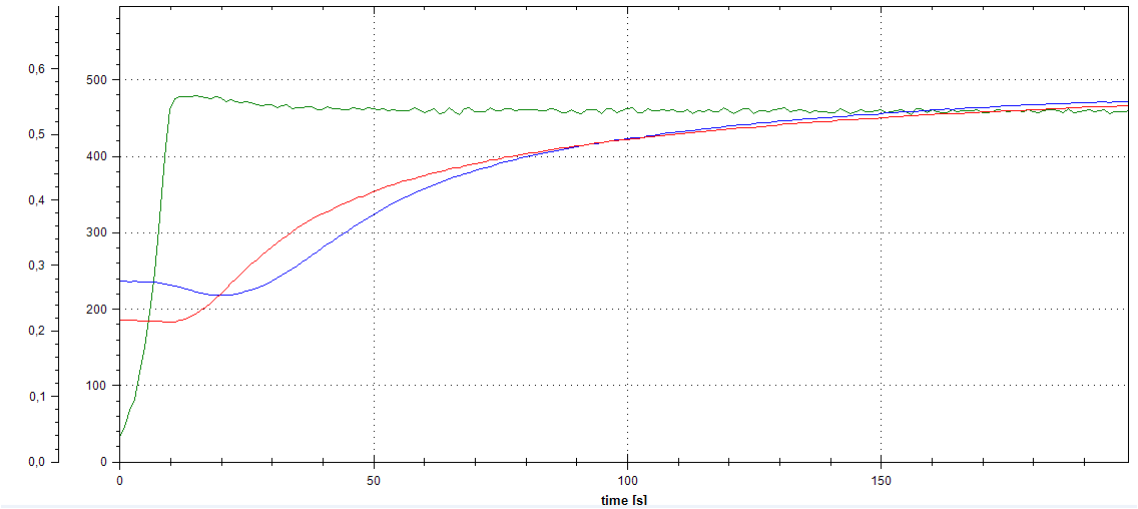

Figure 52: Inlet data given by Volvo Penta showing the inlet temperature (red line), outlet temperature (blue line) and inlet mass flow to the DPF (green line)

5.2.2 Activation Energies and Pre-exponent Multipliers

The results after optimization of the activation energies and pre-exponent multipliers for the oxidation reactions in the DPF are presented in Table (13). The exponent of F is the parameter being optimized in the same way as for the oxidation reactions in the DOC. The result in Table (13) are similar to the same result for the DOC but when calculating the reaction rate coefficient at 373 K the differences are notable. k_m for propylene and diesel fuel are very similar to the DOC results but k_m for CO and NO oxidation are substantially higher for the DPF model than the DOC Table (11), however, since there are many differences between the DOC and the DPF it is reasonable that the values are not equal.

Table 13: Results of optimized values of activation energy and pre-exponent multiplier for oxidation reactions in the DPF and calculated reaction rate coefficient at 373 K

Substance	E_a [J/mol]	F	T [K]	k_m
CO	90122	$10^{14.94} \simeq 8.7 \cdot 10^{13}$	373	209
NO	1901	$10^{4.15} \simeq 1413$	373	7652
$Propylene$	147343	$10^{21.11} \simeq 1.29 \cdot 10^{20}$	373	3
$Dieselfuel$	31888	$10^{5.45} \simeq 28 \cdot 10^{3}$	373	10

5.2.3 CO

When simulating the CO out from the DPF, Ea_{CO} and F_{CO} where manually changed in order to lower the simulated results to match the measured values better at the end of the cycle. Figure (53) represent the result before the change and Figure (54) illustrates the better match of simulated- and measured CO concentration. Ea_{CO} was changed from 90122J/mol to 15000J/mol and the exponent of F_{CO} was changed from 13.94 to 6. This need to change the optimized value could again be explained by the non-uniform inlet gas flow into the DOC, mentioned in earlier chapters. To get a better fit for the kinetic parameters an optimization based on the lower temperature region would probably give better results.

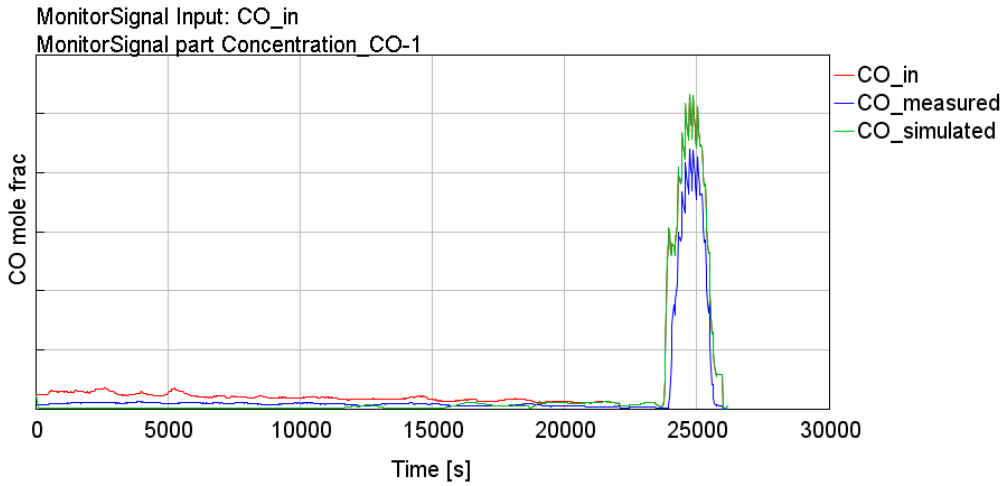

Figure 53: Result of CO simulation versus time, with inlet and measured values for DPF model

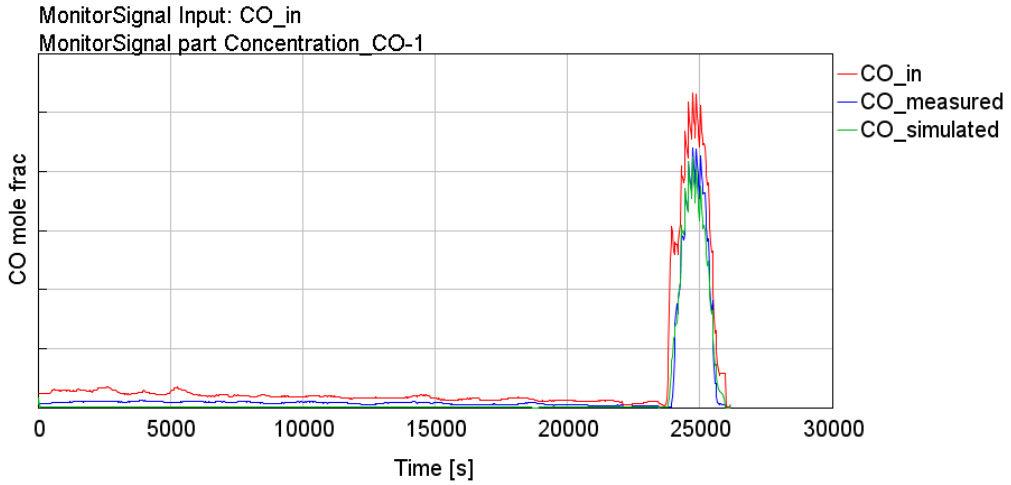

Figure 54: Result of CO simulation after change of activation energy and pre-exponent multiplier for DPF model

5.2.4 HC

The DPF model oxidation of *HC* is presented in Figure (55), where the simulated result, green line, follows the trend, however shifted, of the measured values, blue line, in the beginning of the cycle. At the end of the cycle the inlet concentration increase as do the measured values and the simulated concentration does not increase with the same magnitude, creating a large error to measured values.

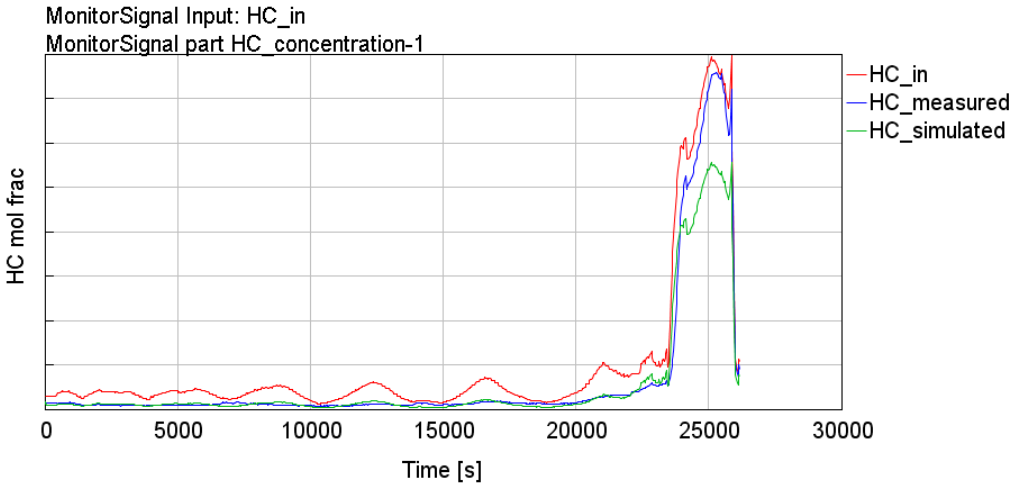

Figure 55: Simulated HC concentration with measured values and inlet concentration for DPF model

In Figure (56) the deviation from measured values are plotted in % for the simulated result on the Y1-axis and the actual difference to the measured values on the Y2-axis. The error shifts between -50% and +50% over the timespan but the actual difference has a maximum value of around 20 ppm, which is not a high value in industrial applications.

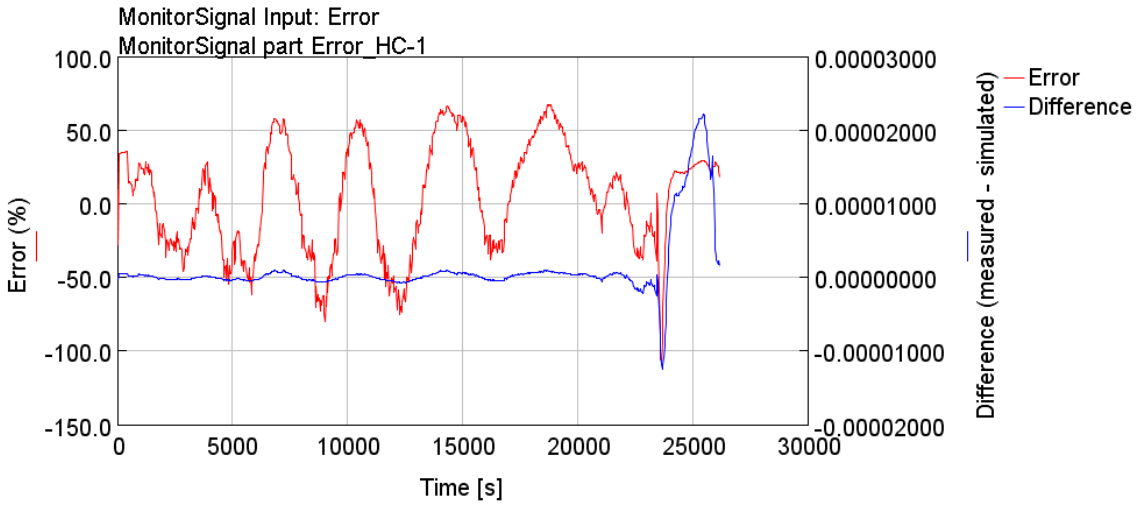

Figure 56: Calculated error and actual difference between simulated and measured result for HC in DPF model

5.2.5 NO

The results for the *NO* oxidation Figure (57) indicates a rather good fit in the beginning of the cycle but at the range between 1900 s to 24000 s that the difference increases as for the DOC model. According to the measured values for this region, there should not be 100% conversion, which the simulated results imply. An optimization based on this region alone (since the optimization was based on the entire cycle) for the kinetic parameters should result in a better fit for the model.

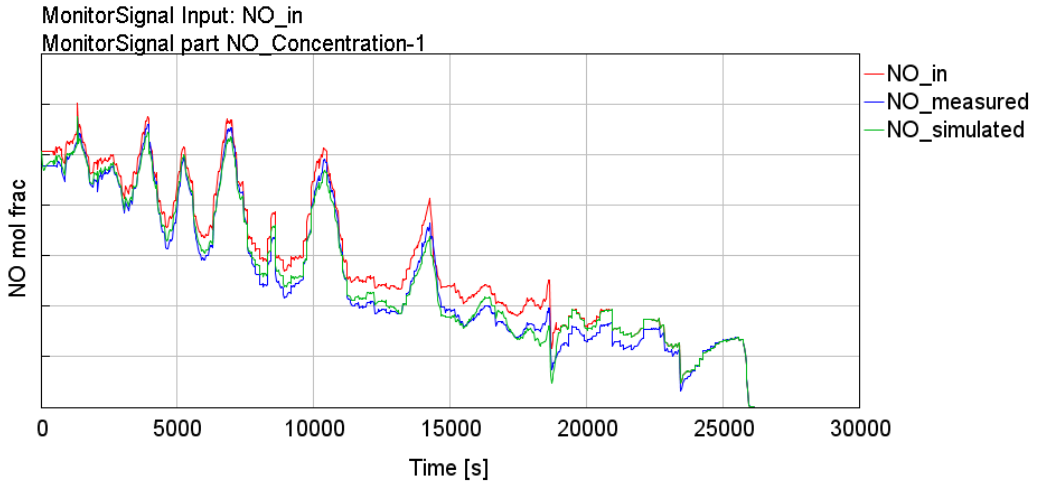

Figure 57: Simulated NO concentration with measured values and inlet concentration for DPF model

The difference between simulated result and measured values of *NO* in the DPF outlet stream is plotted as the blue line in Figure (58). The error in % of measured values is plotted as the red line. Here the point of change at 19000 s is very clear, resulting in large percentage errors. Studying that point in Figure (57) there is a clear fast change in measured concentrations since that corresponds to a decrease in speed.

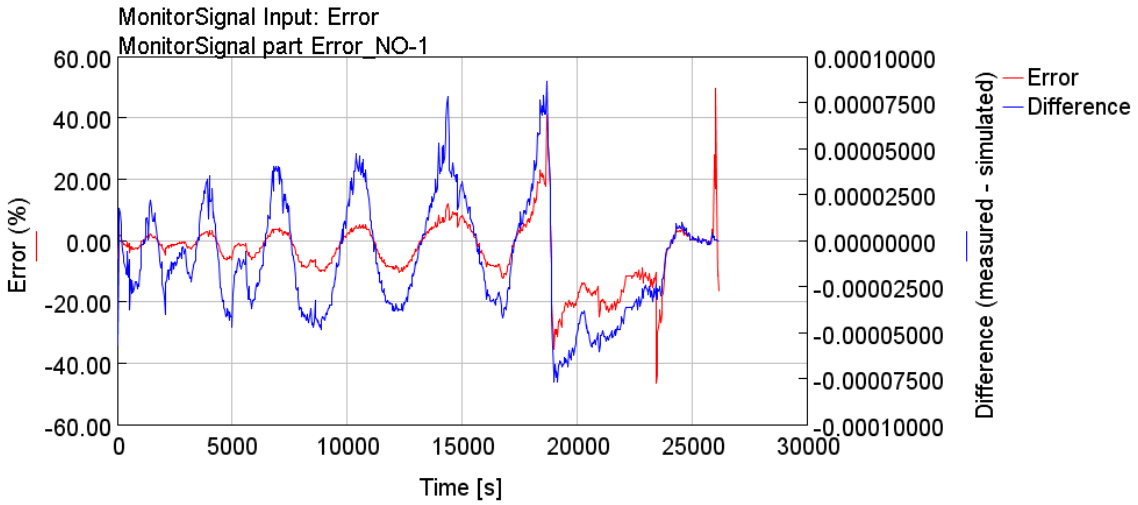

Figure 58: Calculated error and actual difference between simulated NO result and measured NO values out of DPF

5.2.6 Conversion

The conversion of CO, HC and NO oxidation is plotted versus time in Figure (59) and the inlet temperature pink line, is plotted on the Y2-axis. Compared to the DOC model HC conversion does not seem to follow the trend of the inlet temperature, but has a rather low conversion during the whole cycle. Note the low concentration of HC could be a factor to the low conversion, in other words most HC has already undergone oxidation in the DOC. The low HC conversion could also be due to bad measurements resulting in an offset in HC concentration and therefore a bad fitting in the model. The conversion of HC should, at these high temperatures, be much higher.

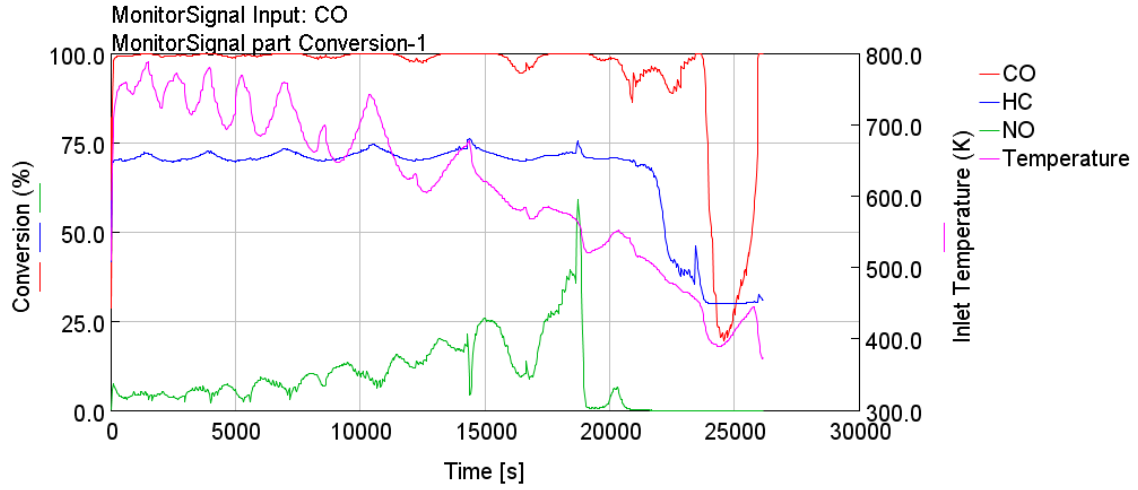

Figure 59: Conversion of CO (red), HC (blue) and NO (green) and inlet temperature K.

5.2.7 Pressure Drop

The optimization of initial soot loading gave the results seen in Table (14). The calculated initial soot load can also be seen and the difference is rather large. Firstly it is worth mentioning that it is ambiguous to optimize the pressure drop since there are two phenomena's influencing it, Figure (22). Second the calculated initial soot loading in Table (14) is miscalculated with a factor of 10 when converting the units from liter to m^3 which was discovered too late in the project. The initial guessed value based on 2g/L of soot would result in 48 g in total. Studying Figure (22) that would give an initial guess of about 40 g in the cake layer and 8 g in the wall layer. Looking at the contour plot of the optimization Figure (60), the initial calculated case at 4.8 g vs 0 g seems to be in the lower region of the error of pressure drop, the dark blue region. The optimized values in the contour plot at 9.91 g vs 2.18 g is also situated in the low error region. However it seems the optimization has not converged and that the value for the initial cake layer should be higher, which is in line with the correct calculation with a higher total soot load. Nevertheless it is interesting that the error is still at the low region despite the incorrect guessed and optimized values and the model produced a good simulation of the pressure drop.

Table 14: Calculated and optimized initial soot load division between the wall and cake layer

Initial soot load	Calculated	Optimized
In wall layer [g]	4.8	2.18
In cake layer [g]	0	9.91

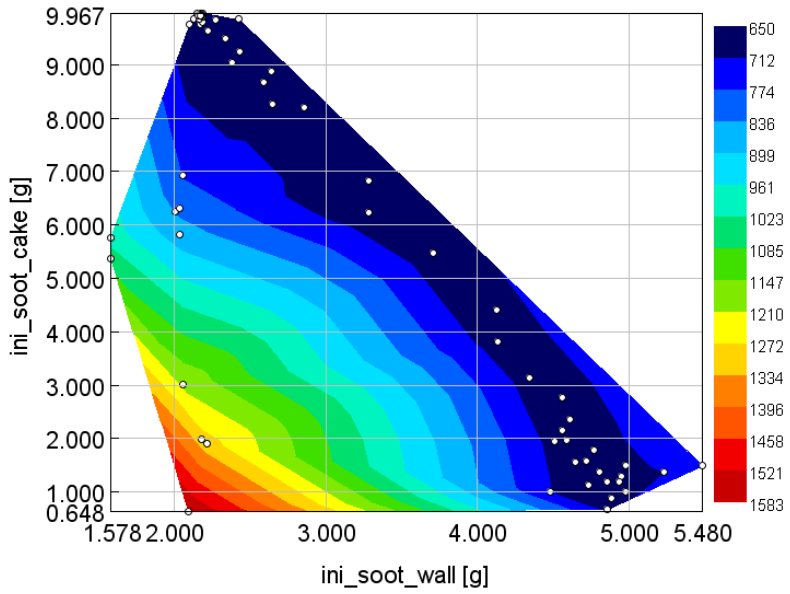

Figure 60: Optimization of initial soot loading in wall- and in cake layer versus integrated $SSE_{Pressure_drop}$ color gradient.

The pressure drop over the DPF is one of the most interesting parameters. With the optimized initial soot loading it is presented in Figure (61). There are still some differences remaining, especially at the two highest pressure drop points with 0.6 and 0.57 kg/s of inlet mass flow respectively, Figure (24a). Overall the simulation of the pressure drop is good so the calculations based on the parameters from Table (5) appear to be the right approach for simulating the pressure drop, even though the guessed initial soot loading was incorrect.

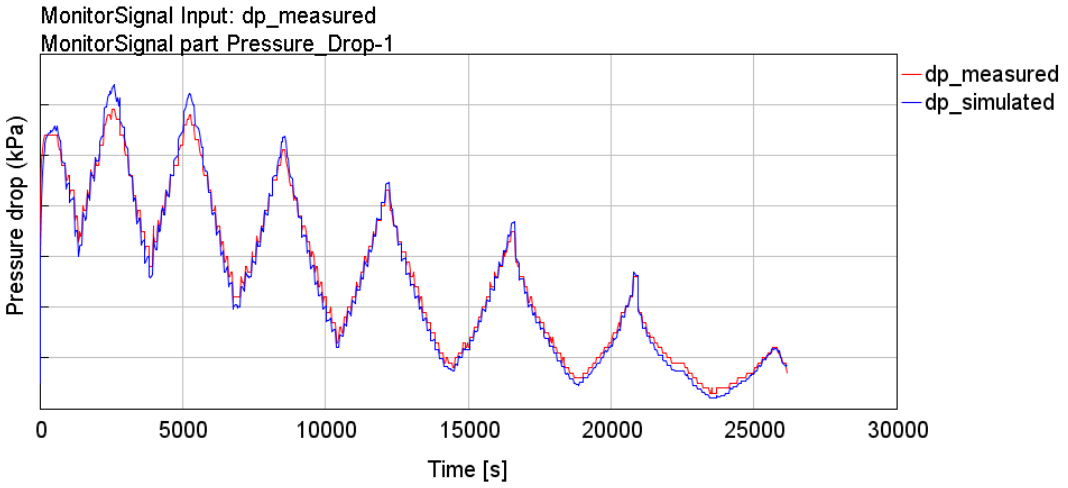

Figure 61: Simulated and measured pressure drop dp, over the DPF

Figure (62) illustrates the difference between simulated- and measured pressure drop. The deviation from measured values in % of simulated results, the red line is plotted on the Y1-axis. The actual difference, blue line, is plotted against the Y2-axis. At the end of the cycle a large error of about 40% occurs but this only gives an actual difference of about 0.1 kpa pressure drop. Looking at the high temperature and high mass flow rate region in Figure (62), two large peaks giving about 0.5 kpa in actual difference occur which is the two points with mass flow rates of 0.6 and 0.57 kg/s mentioned above.

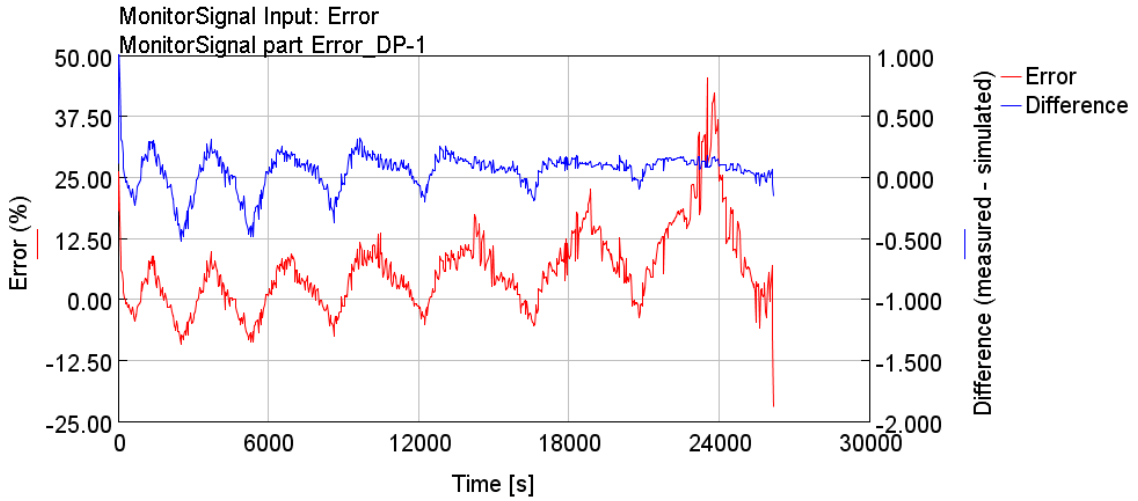

Figure 62: Calculated error and actual difference between simulated pressure drop and measured pressure drop over the DPF

As seen in Figures (63a) and (63b) the permeability through the cake layer and the wall layer of the DPF decreases over time. In the soot cake layer the permeability changes however, almost according to the trend of the temperature. This indicated that soot is oxidized and the permeability increases, when the temperature increases. The permeability of the wall seems to decrease more drastically at the beginning when the soot is loaded and then subsides at the end of the cycle.

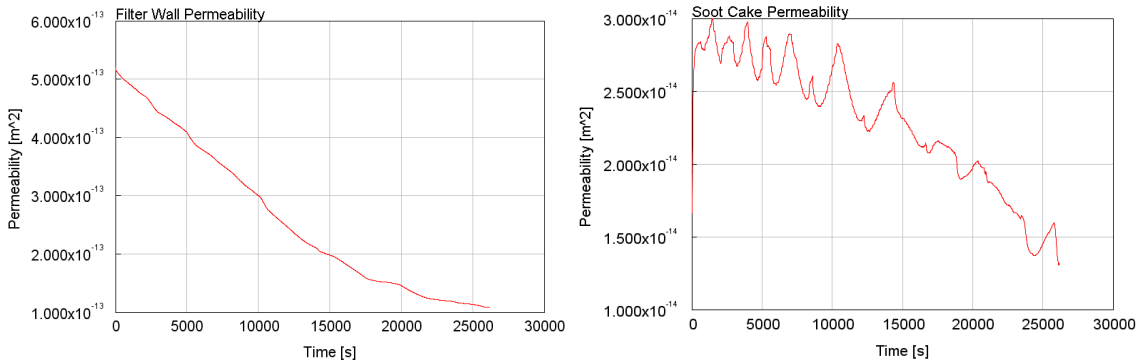

(a) Permeability m^2 in wall layer versus time s

(b) Permeability m^2 in cake layer versus time s

Figure 63: Change of permeability in DPF model for both cake- and wall layer

5.2.8 Validation

The Validation of the DPF model was done using the NRTC according to parameters from Table (8) and it resulted in similar trends as the PLM cycle. Unfortunately it seems that the measurements of the NRTC were not activated until about 1000 s into the cycle. This is shown best when looking at the temperature, Figure (64). The measured temperature, the blue line, is constant in the beginning and then abrupt drops before increasing rapidly again, indicating errors in measurements.

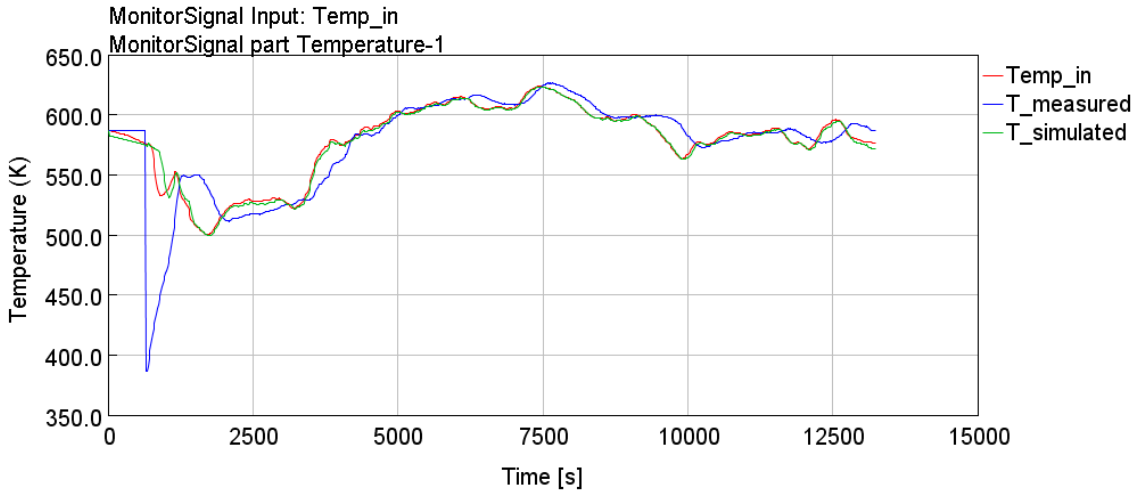

Figure 64: Simulated temperature for validation of DPF model

Studying the pressure drop in Figure (65) the simulation results shows the same trends as for the PLM cycle. The largest shortcomings is in the beginning of the cycle, which could be due to unknown initial soot load.

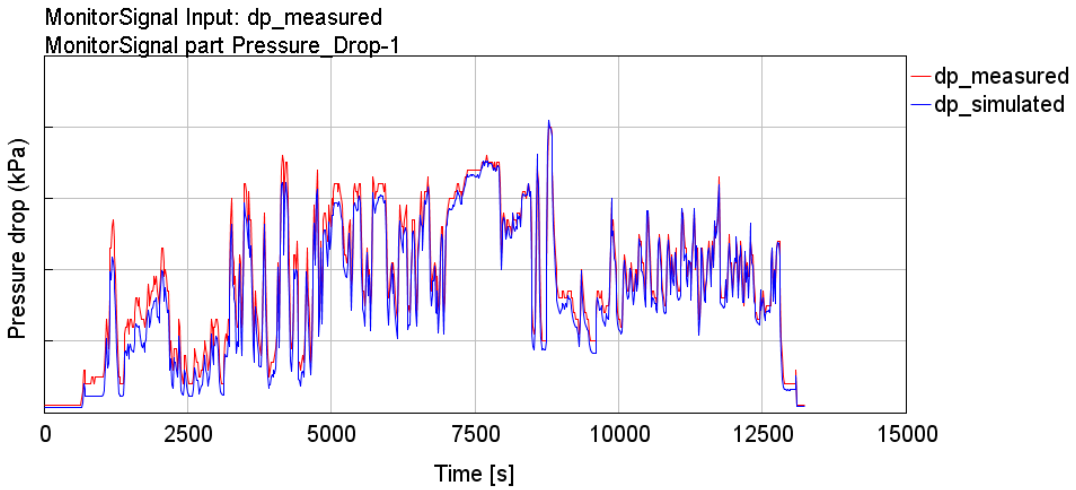

Figure 65: Simulated pressure drop for validation of DPF model

The rest of the figures for the validation of the DPF model is shown in Appendix 2.

5.3 DOC+DPF

The DOC and the DPF models were combined and tested with a C1 cycle and a NRTC cycle.

5.3.1 C1

The simulation for the combined model had a lot of shortcomings compared to the measured values, for CO, HC and NO concentration. Looking at the simulation for NO seen in Figure (66) is seems to be at high torque that the model simulates a better fit, especially at high speed, Figure (28). The reason for concentrations dropping to zero in between peaks is that the measurements are taken at 8 steady state points.

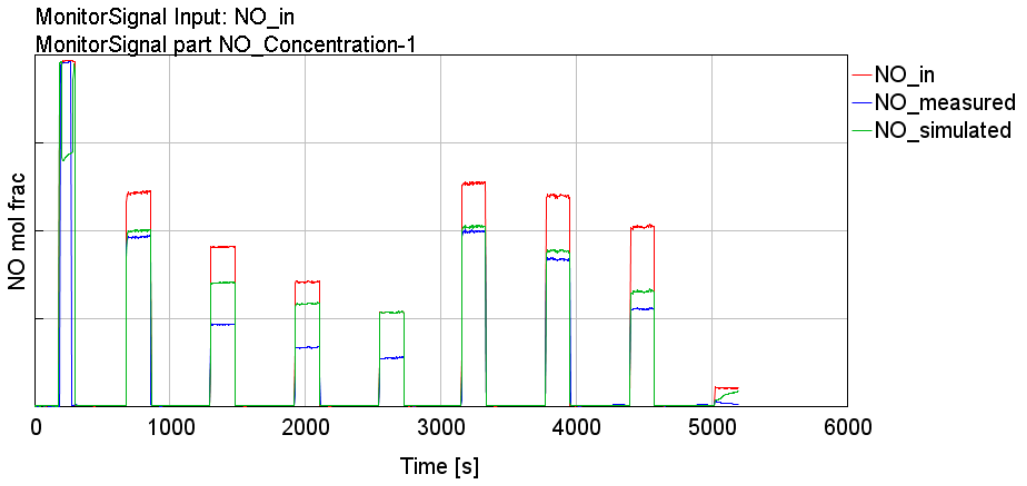

Figure 66: Simulated NO over DPF with C1 cycle for the DOC+DPF model

The pressure drop simulation over the DPF in the DOC+DPF model is not very accurate, see Figure (67). The values of the simulated results are almost double the measured values. This strengthens the conclusion of how the initial soot load of the DPF is important to know or at least the information of how the system had been run previously to indicate a better initial soot load guess.

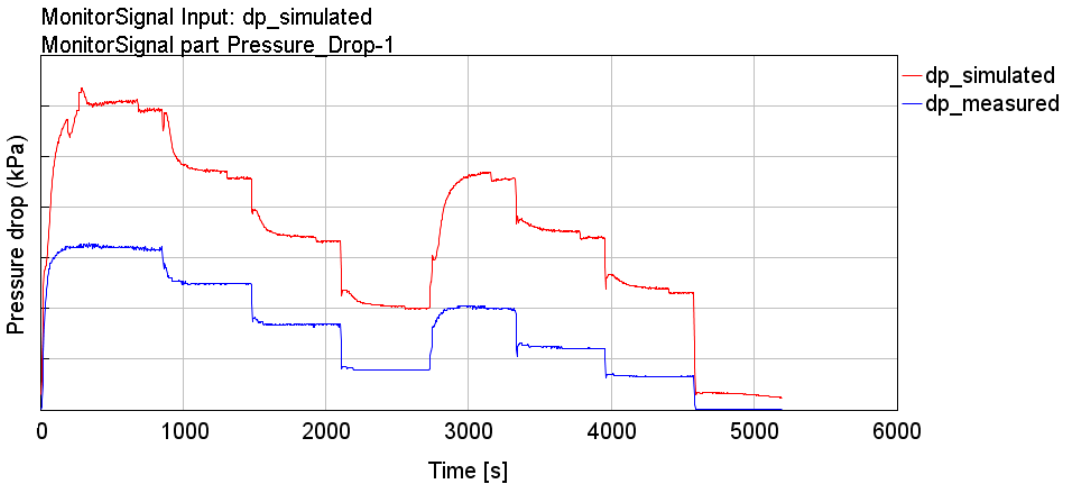

Figure 67: Simulated pressure drop over DPF with C1 cycle for the DOC+DPF model

5.3.2 NRTC

The NRTC test showed better results than the C1 cycle for the combined model, especially in terms of pressure drop. Looking at the simulated NO concentration in Figure (68) it indicates that Ea_{NO} is too large since the simulated result are higher than the measured values throughout the cycle. The results for the CO oxidation Figure (85) implies yet again that the gas flow inlet is not uniform, since there is a measured CO slip at high temperatures. The simulation for HC has big errors, however, looking at the actual differences in Figure (86b) it has a maximum of around 8 ppm which is very low. Also when comparing the outlet values for both measured and simulated concentration against inlet concentration in Figure (86a), the conversion of the model is in the same range as the measured conversion. The pressure drop is shown in Figure (69) with a maximum error of approximately 1 kpa.

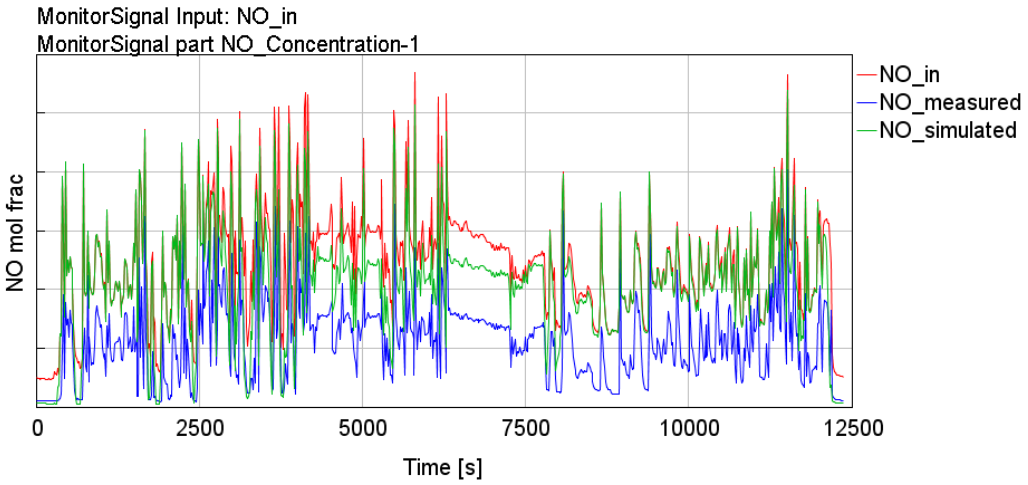

Figure 68: Simulated NO over DPF with NRTC for the DOC+DPF model

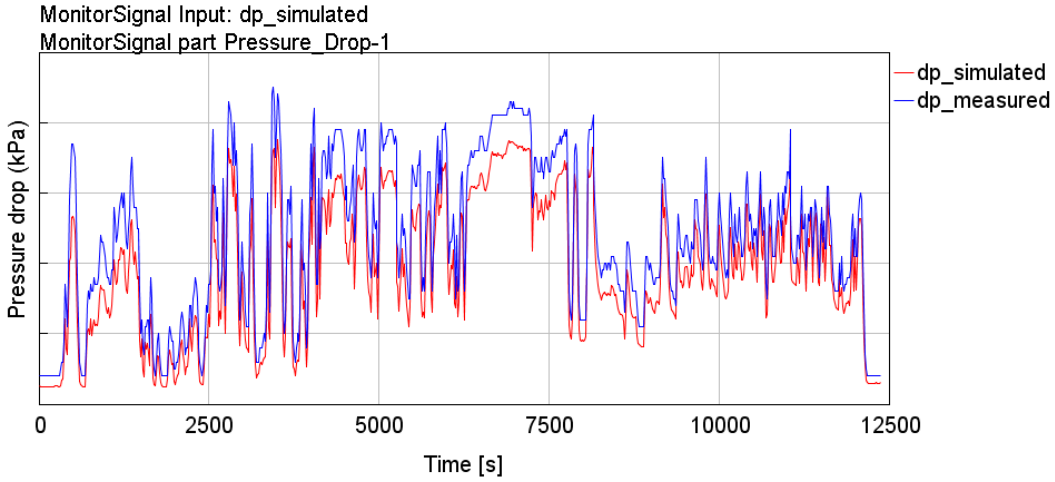

Figure 69: Simulated pressure drop over DPF with NRTC for the DOC+DPF model

Overall, the combined model showed good results for the NRTC cycle. However, if Ea and F had been optimized for the lower temperature region, the results would probably be even more accurate.

6 Analysis

Comparing the DOC results for E_a and F to literature values they differ significantly. However, so does also the values between different literature sources as well, so the results of E_a and F should not be disregarded. Rather can the conclusion that finding a simple model valid for all types of cases is difficult.

An initial assumption made by the model concerns the inlet pipe to the DOC. According to Figure (1) the inlet pipe has almost a 90° bend towards the DOC, however looking at Figure (2), the modeled inlet pipe is straight. Consequently high exhaust gas flow will not disperse evenly over the DOC surface. The non-uniform velocity could influence the temperature, creating a gradient over the channels. Since the measured values indicates CO slip out from the DOC at high temperature, where CO normally would react, this uneven distribution of gas is a key source of error. The CO at the side of the DOC with higher gas flow, indicated by red in Figure (39), would not react since the residence time would be low, hence increase the outlet concentration of measured CO. The model however, shows a higher conversion at the high temperatures for CO, which could be described by the straight inlet pipe modeled and the uniform channel distribution of exhaust gas.

At high temperatures it is often mass transport that govern the reaction rates and not the kinetics. Therefore are the reactions at high temperatures, more affected by mass transfer resistance than kinetics. The kinetics would therefore be better optimized during the lower temperature part of the cycle, were the reaction rate is more dependent on kinetics than mass transport. Nevertheless the optimization for E_a and F were conducted based on the hole cycle giving inaccurate kinetic parameters. Looking at the results for NO oxidation for the DOC model and the DPF model, they are better in the beginning and middle of the cycle, however, when the temperature decreases and the kinetics govern the reactions, the errors increase. To get the best fit for the NO, CO and HC oxidation a fixed temperature interval were the kinetics is the time dependent step should be used to tune Ea and F and a variation of inhibition functions should be analyzed.

Since temperature affects all the reactions according to Equation (12), it would have been better to optimize h and the air thickness layer before optimizing E_a and F. On the other hand, the reactions also affect the temperature, and therefore the heat loss parameters but probably not in the same magnitude since the concentrations are so small. An assumption made in the model was that the air thickness layer is uniform around the substrates which it is not. An optimized value for the air thickness layer gives an average in meter. This air thickness value affects the heat loss and thus the temperature. The air in the air layer is also modeled as ambient air but in reality that air has a higher temperature due to heating from other parts of the catalytic muffler.

The channels in the DOC were assumed to be square with perfect uniform packing of washcoat. However, according to Figure (6a) the washcoat thickness is often larger in the corners and thinner at the sides. This non-uniformity of the coated washcoat layer creates not perfect square channels, but they become more circular. This difference affects the Nu number, Sh number and f_fRe number. Changing the dimensionless numbers changes the heat-and mass transfer coefficients, which affect resistance and thus conversion. A study for different dimensionless numbers would give a better understanding of how the reality and theory is coupled.

The unknown initial soot loading in the DPF is a problem when optimizing the pressure drop. Studying the contour plot Figure (60) the change in $SSE_{pressure_drop}$ might not be so big between the miscalculated initial guess and the optimized value, since both are in the dark blue area of the graph. A set of test cell data with initial clean filter and no engine coupled to the muffler would be ideal to measure initial pressure drop over the DPF. If that cannot be provided, information about previous cycle run on the system is crucial to guess initial soot loading better.

Looking at the values for outlet concentration of CO, HC and NO the general amount is just a few ppm. For an industrial perspective a value of around 10 ppm is so low that it can be re-

garded as measurement error. The focus should lie on high concentration parts of the cycles and getting accurate conversions, to make a statement about the model, not absolute numbers.

7 Conclusions

The goal of this thesis project was to evaluate the 1D modeling methodology for Exhaust gas aftertreatment system (EATS) based on experimental data for the purpose of engine system virtual calibration. Two models were designed, one for DOC and one for DPF and those models were then combined and evaluated. The work focused on creation and evaluation of the simulation models for Diesel Oxidation Catalyst (DOC) and Diesel Particulate Filter (DPF), as well as their combination.

The temperature over the DOC and DPF was modeled based on several approximations of insulation, kinetics, e.g. The insulation affects the heat loss and thereby the temperature, which in turn influences the reaction kinetics. Two parameters selected for optimization were activation energy and external heat transfer coefficient both influencing the temperature. It should be noted that these two parameters were not optimized simultaneously to save time, but since they affect each other, optimizing them at the same time would probably lead to more accurate results. In the DPF, the soot oxidation affects the pressure drop and it was optimized by changing the initial soot loading. The initial soot load is, however, individual for each run, hence a more suitable approach would be to optimize the DPF by first knowing the initial soot load from test cell data and then tuning the kinetics. By optimizing all the selected parameters over the entire test cycle, the PLM, various differences between simulated and experimental data arose. At the beginning of the cycle were the temperature and mass flow were high, the parameters were optimized to increase the simulated concentrations to meet the measured result. This resulted in large errors in the latter part of the cycle, were the temperature and mass flow were lower and the simulated result higher than the measured values. In conclusion, if the kinetic parameters would have been optimized based only on the last part of the cycle, were it is most difficult to capture the accurate reaction rate, it would probably result in a more accurate model. This assumption was confirmed using the combined DOC-DPF model for the C1 and NRTC over the lower temperature region, were the torque and speed were both low. The model validation also showed more accurate results for the transient NRTC and PLM cycles than for the steady-state C1 cycle.

Future work should consider the optimization of the kinetics in different temperature regions. Optimizing all the parameters affecting the temperature simultaneously would also be of interest. Furthermore, the pressure drop simulation could be improved if the initial soot load was known in advance.

8 References

Bibliography

Aberg, A., Widd, A., Abildskov, J. and Huusom, J. K. (2016), 'Parameter estimation and analysis of an automotive heavy-duty scr catalyst model', *Elsevier, Chemical Engineering Science, http://www.sciencedirect.com.proxy.lib.chalmers.se/science/article/pii/S0009250916306777?*$_r doc = 1_f mt = high_o rigin = gateway_d ocanchor = md5 = b8429449ccfc9c30159a5f9aeaa92ffb$.

Andersson, J. (2006), 'Deactivation of diesel oxidation catalysts', *Department of applied physics, Chalmers University of Technology, Main Library Chalmers Johanneberg* .

Busca, G. (2014), 'Heterogeneous catalytic materials, solid state chemistry, surface chemistry and catalytic behaviour', *Elsevier, http://www.sciencedirect.com.proxy.lib.chalmers.se/science/book/9780444595249* pp. 1–7.

Creaser, D. (2017), 'Advanced chemical reaction engineering', *Course material, Chalmers University of Technology* .

Dieselnet (2017), 'https://www.dieselnet.com/standards/eu/nonroad.php'.

Engineeringtoolbox (2017), 'http://www.engineeringtoolbox.com'.

Fino, D. (2006), 'Diesel emission control: Catalytic filters for particulate removal', *Elseiver, Science Direct, http://www.sciencedirect.com/science/article/pii/S1468699606002294, 2017-07-20* .

GammaTechnologies (2017*a*), 'Gt-suite exhaust aftertreatment application manual', *GT-SUITE software* .

GammaTechnologies (2017*b*), 'https://www.gtisoft.com/'.

Hidemitsu, H. and Shuichi, K. (2008), 'Computer simulation study on filtration of soot particles in diesel particulate filter', *Elseiver, http://www.sciencedirect.com/science/article/pii/S0898122107006396, 2017-07-20* .

Johnsson, T. V. (2011), 'Diesel emissions in review', *Corning inc SAE international, doi:10.4271/2011-01-0304* .

Lohse, H. W. (1945), 'Catalytic chemistry', *Chemical publishing, https://babel.hathitrust.org/cgi/pt?id=mdp.39015065776174;view=1up;seq=6* .

Lundberg, B., Sjoblom, J., Johansson, A., Westberg, B. and Creaser, D. (2016), 'Doc modeling combining kinetics and mass transfer using inert washcoat layers', *Applied Catalysis B: Environmental* **191, 0926-3373**, 116–129.

Majewski, W. and Khair, M. K. (2006), *Diesel Emissions and Their Control*, SAE international, ISBN 9780768049749, 0768049741.

Naturvårdsverket (2017), 'http://www.naturvardsverket.se/sa-mar-miljon/statistik-a-o/kvaveoxid-till-luft/'.

Ratcliff A, M., Dane, A. J., Williams, A., Ireland, J., Luecke, J., Mccormick, R. L. and Voorhees, K. J. (2010), 'Diesel particle filter and fuel effects on heavy-duty diesel engine emissions', *American Chemical Society, http://pubs.acs.org.proxy.lib.chalmers.se/doi/abs/10.1021/es1008032* .

Sampara, C. S., Bissett, E. J. and Chmielewski, M. (2007), 'Global kinetics for a commercial diesel oxidation catalyst with two exhaust hydrocarbons', *American Chemical Society, Industrial and Engineering Chemistry Research, http://pubs.acs.org.proxy.lib.chalmers.se/doi/abs/10.1021/ie070813x* .

Sampra, C. S., Bissett, E. J. and Assanis, D. (2008), 'Hydrocarbon storage modeling for diesel oxidation catalysts', *Elseiver, http://www.sciencedirect.com.proxy.lib.chalmers.se/science/article/pii/S0009250908003333* .

Stratakis, G. A., Psarianos, D. L. and Stamatelos, A. M. (2002), 'Experimental investigation of the pressure drop in porous ceramic diesel particulate filters', *SAGE publications, http://journals.sagepub.com.proxy.lib.chalmers.se/doi/abs/10.1243/0954407020603408 62* .

Voltz, S. E., Morgan, C. R., Liederman, D. and Jacob, S. M. (1973), 'Kinetic study of carbon monoxide and propylene oxidation on platinum catalysts', *Ind. Eng. Chem. Prod. Res. Develop* .

Wang-Hansen, C. (2012), 'Kinetic analysis of automotive soot oxidation', *Department of Chemical and Biological Engineering Chalmers University of Technology, Volume 3406, ISBN 9789173857253, 9173857254* .

Welty, J., Wicks, C., Wilson, R. and Rorrer, G. (2008), 'Fundamentals of momentum, heat, and mass transfer 5:th edition', *Daniel Sayre* .

Ye, S., Yap, Y. H., Koalczkowski, S. T., Robinson, K. and Lukyanov, D. (2011), 'Catalyst 'light-off' experiments on a diesel oxidation catalyst connected to a diesel engine - methodology and techniques', *Elsevier B.V., Chemical Engineering Research and Design, 2012* .

Zhang, F., Hayes, R. and Kolaczkowski, S. (2004), 'A new technique to measure the effective diffusivity in a catalytic monolith washcoat', *Elseiver, http://www.sciencedirect.com.proxy.lib.chalmers.se/science/article/pii/S0263876204725174?*$_{r}doc = 1_{f}mt = high_{o}rigin = gateway_{d}ocanchor = md5 = b8429449ccfc9c30159a5f9aeaa92ffbccp = y.$

Appendix

Appendix 1 Nomeclature

t	Time [s]
υ	Velocity [m/s]
z	axial length [m]
Ψ_s	Effective heat capacity [J/m^{3}K]
T_s	Temperature of gas at catalyst surface - solid phase temperature [K]
f_{sb}	Solid fraction of substrate
λ_{sb}	Thermal conductivity of substrate [J/m s K]
h	Heat transfer coefficient [W/m^{2}K]
S	Surface area per reactor volume [m^{-1}]
T_g	Temperature of bulk gas in reactor channels [K]
ΔH_j	enthalpy of reaction j [J/mol]
r_j	Reaction rate of reaction j [mol/m^{3}s]
P	Power input [J/s]
V	Reactor volume [m^3]
S_x	External surface area per reactor volume [m^{-1}]
T_x	External temperature [K]
ε	Void fraction of reactor
ρ_g	Density of bulk gas in reactor channels [kg/m^3]
C_{pg}	Heat capacity of gas [J/kg K]
ω_g	Mass fraction in bulk phase
$k_{m,i}$	Mass transfer coefficient for species i [kg/m^{2}s]
ω_s, i	Mass fraction at the surface of species i
N	Total number of reactions
$\sigma_{i,j}$	Stoichiometric coefficient for species i in reaction j
p	Pressure [Pa]
ϵ	Washcoat porosity
f_f	Friction factor
k	Reaction rate coefficient [mol/m^{3}s]
C	Concentration [mol/m^3]
β	Order of reaction
G	Inhibition function
F	Pre-exponent multiplier
E_a	Activation energy [J/mol]
R	Gas constant [J/mol K]
a_j	Active site density for reaction j [mol-site/m^3]
A_k	Active site density for coverage k [mol-site/m^3]
θ	Coverage
N_i	Molar flux of species i [mol/m^{2}s]
Nu	Nusselt number
Sh	Sherwood number
Re	Reynolds number
Pr	Prandtl number
Sc	Schmidt number
D_h	Hydraulic diameter of channel [m]
λ_g	Thermal conductivity of gas [J/m s K]
D_p	Pore diameter [m]
$D_{i,m}$	Binary diffusion coefficient of trace species in the mixture [m^2/s]
μ	Gas viscosity [Pa s]
D_{eff}	Effective diffusivity [m^2/s]
τ	Washcoat tortuosity

D_{gas}	Species diffusivity calculated from Fuller correlation [m^2/s]
D_{Kn}	Knudsen diffusivity [m^2/s]
d_{pore}	Washcoat pore diameter [m]
$\overline{r_j}$	Average reaction rate for reaction j [mol/m^3s]
δ	Washcoat thickness [m]
f_{wc}	Solid fraction of washcoat
ρ_s	Density of gas at catalyst surface [kg/m^3]
R_i	Species mass rate [kg/m^3s]
M_i	Molecular weight of species i [kg/mol]
K_{eq}	Equilibrium constant
K_c	Calculated reaction constant
κ	Permeability
ξ	Pressure drop coefficient
Q	Volumetric flow rate [m^3/s]
w_{wall}	wall layer thickness [m]
w_{soot}	soot cake layer thickness [m]
$w_{slab,i}$	Thickness of each discretization slab in the DPF layer [m]
D	Channel width [m]
α_i	Forchheimer constant in layer i [1/m]
H	Channel pressure drop correlation = 28.454
L	Channel length [m]
V_{trap}	Total filter volume [m^3]
$v_w, 1$	Velocity at soot layer inlet [m/s]
$v_w, 2$	Velocity at substrate wall [m/s]
W	Weight function

Appendix 2 Results

Validation of DPF

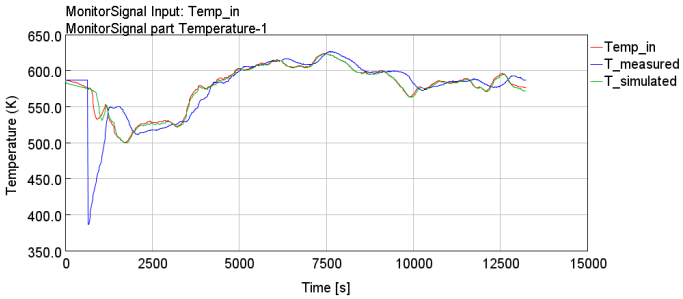

(a) Temperature

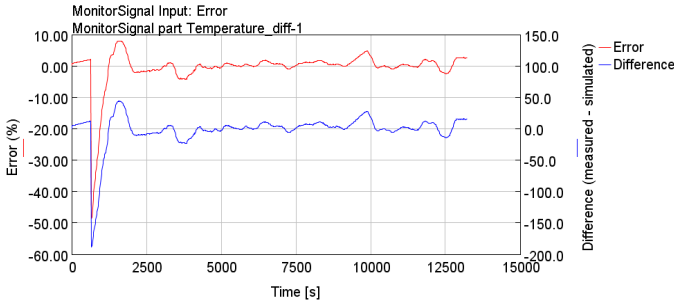

(b) Error of Temperature

Figure 70: Temperature simulation with NRTC for DPF

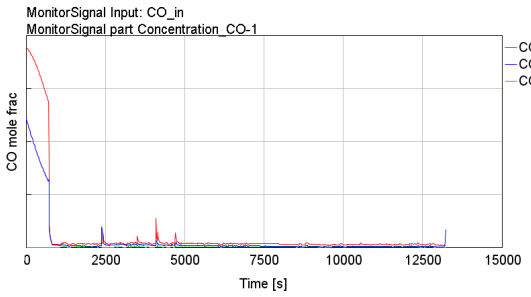

(a) CO

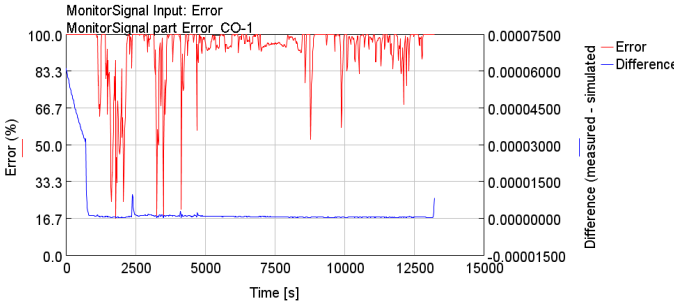

(b) Error of CO

Figure 71: CO simulation with NRTC for DPF

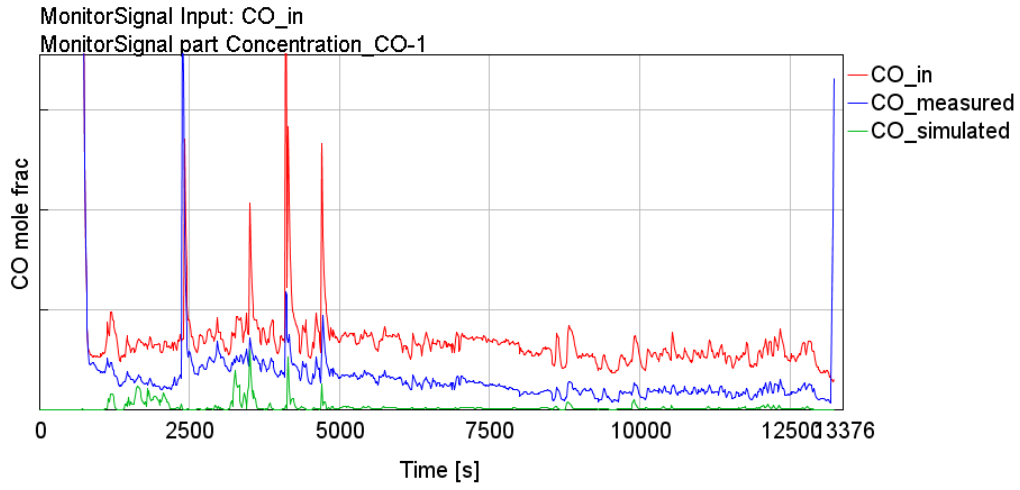

Figure 72: Zoomed CO concentration with NRTC for DPF

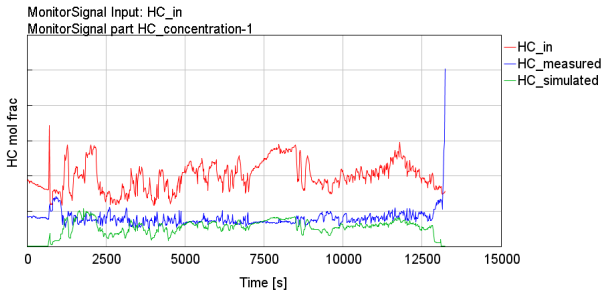

(a) HC

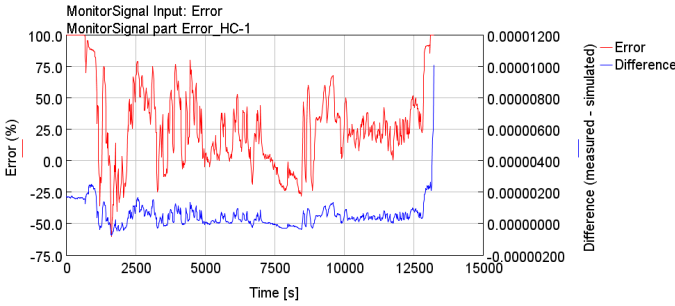

(b) Error of HC

Figure 73: HC simulation with NRTC for DPF

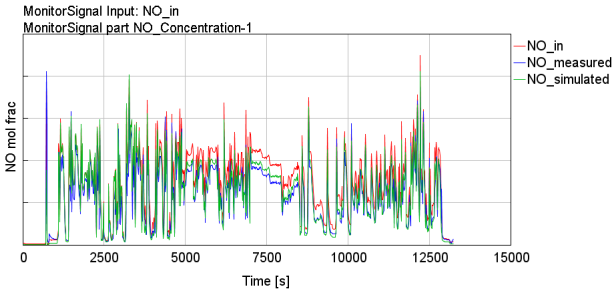

(a) NO

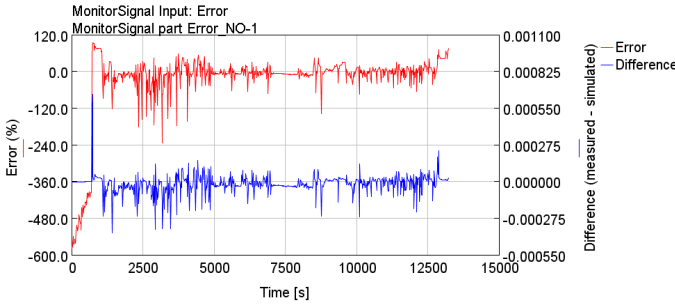

(b) Error of NO

Figure 74: NO simulation with NRTC for DPF

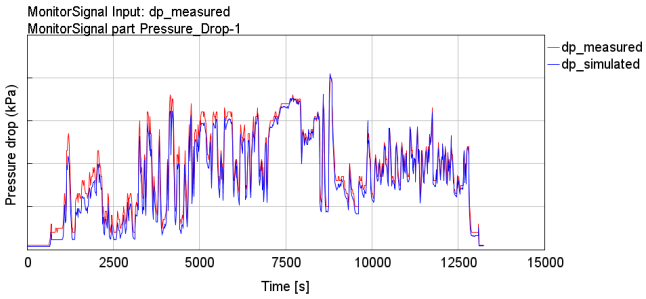

(a) Pressure drop

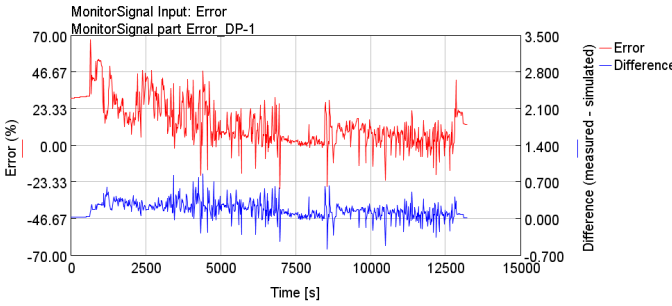

(b) Error of pressure drop

Figure 75: Pressure drop simulation with NRTC for DPF

DOC+DPF C1

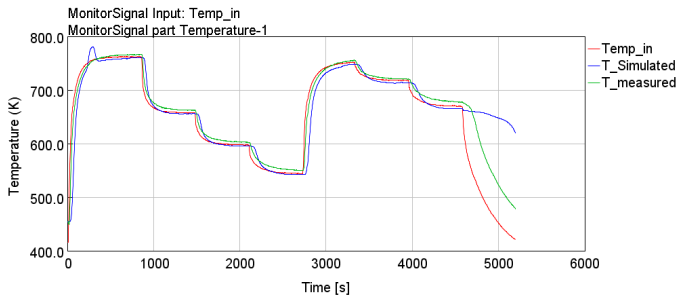

(a) Temperature

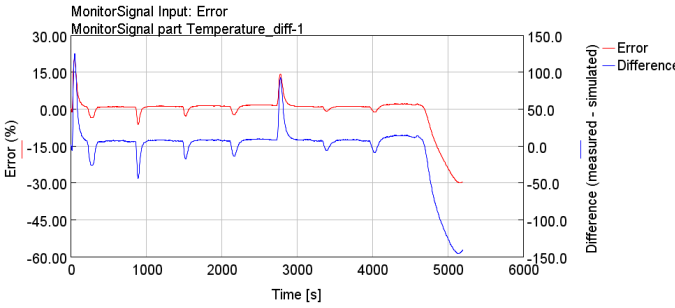

(b) Error of Temperature

Figure 76: Temperature simulation with C1 cycle for DOC+DPF

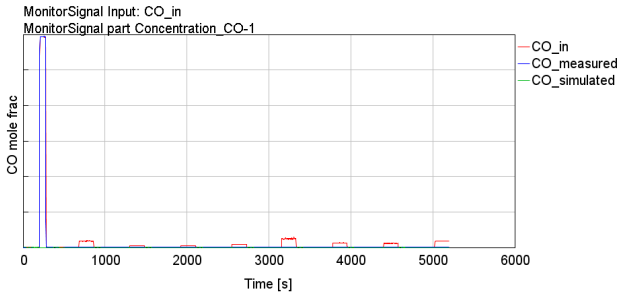

(a) CO

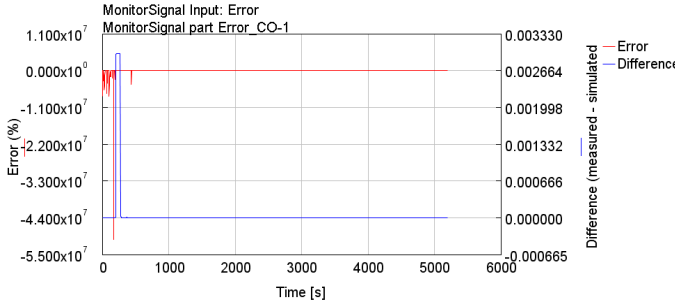

(b) Error of CO

Figure 77: CO simulation with C1 cycle for DOC+DPF

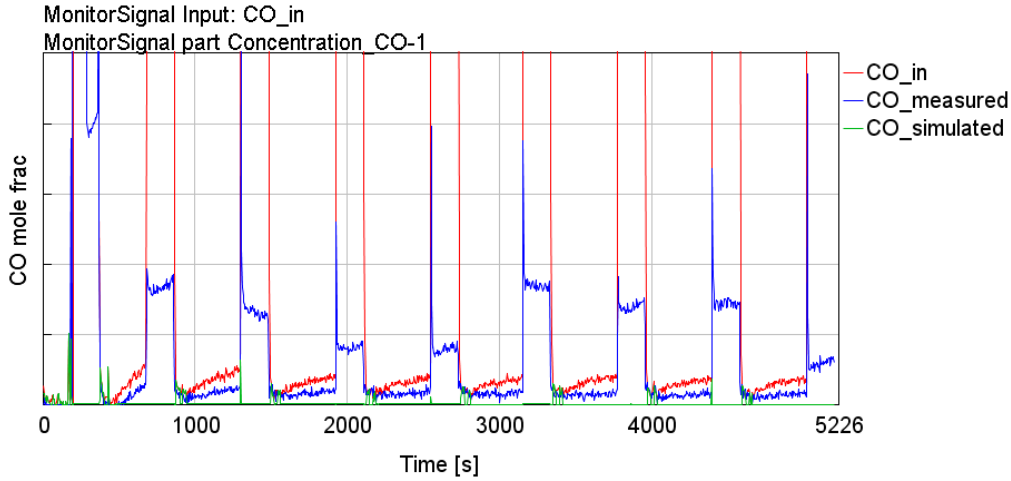

Figure 78: Zoomed CO concentration with C1 cycle for DOC+DPF

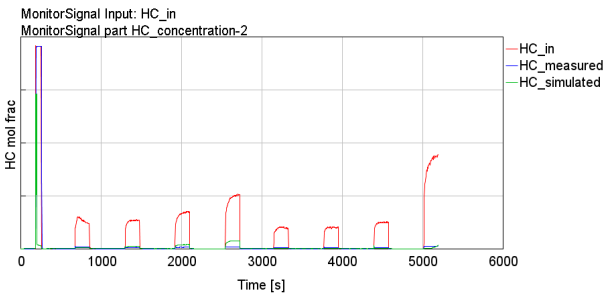

(a) HC

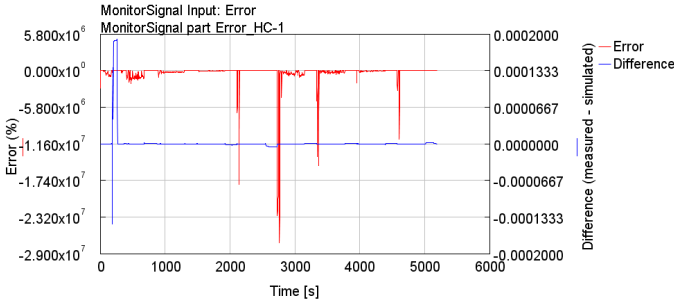

(b) Error of HC

Figure 79: HC simulation with C1 cycle for DOC+DPF

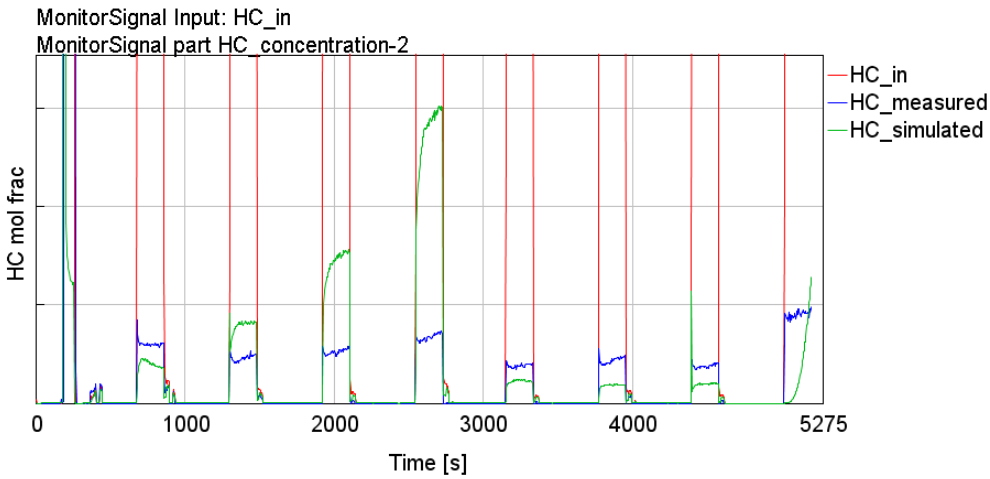

Figure 80: Zoomed HC concentration with C1 cycle for DOC+DPF

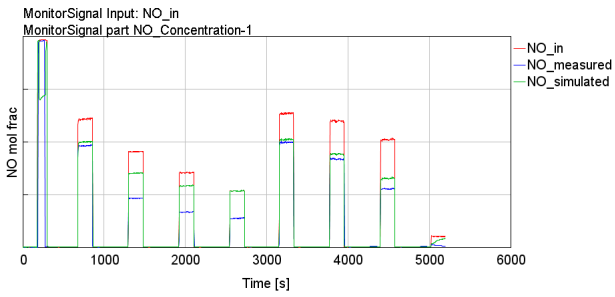

(a) NO

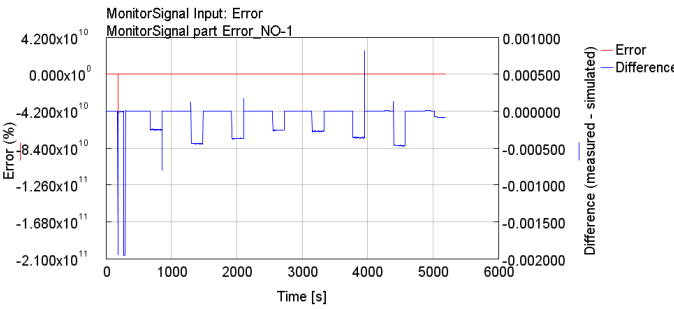

(b) Error of NO

Figure 81: NO simulation with C1 cycle for DOC+DPF

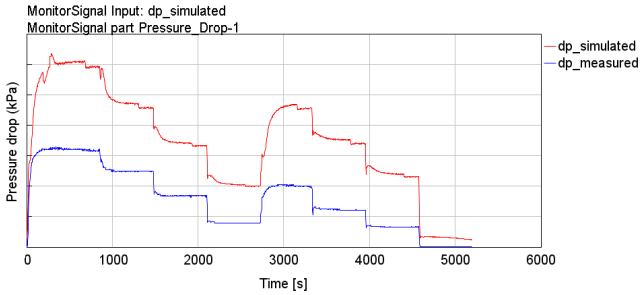

(a) Pressure drop

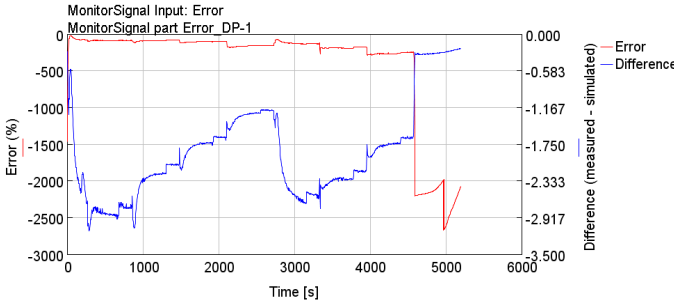

(b) Error of pressure drop

Figure 82: Pressure drop simulation with C1 cycle for DOC+DPF

DOC+DPF NRTC

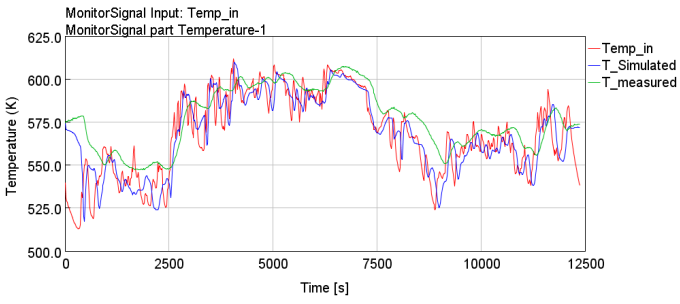

(a) Temperature

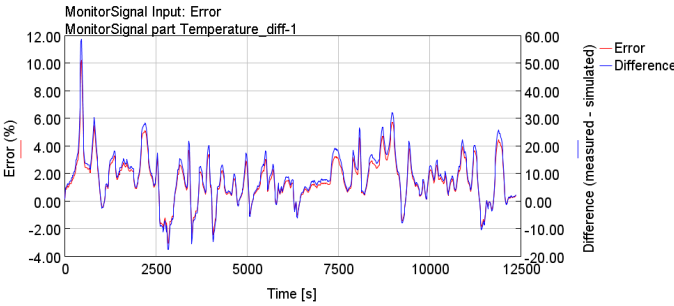

(b) Error of Temperature

Figure 83: Temperature simulation with NRTC for DOC+DPF

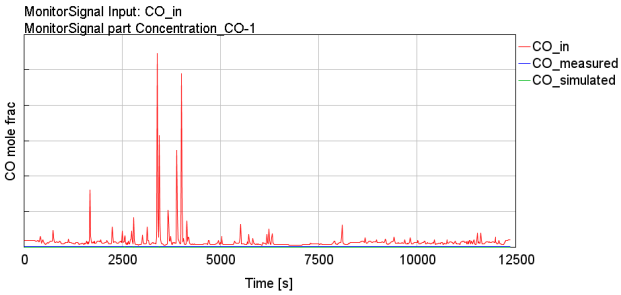

(a) CO

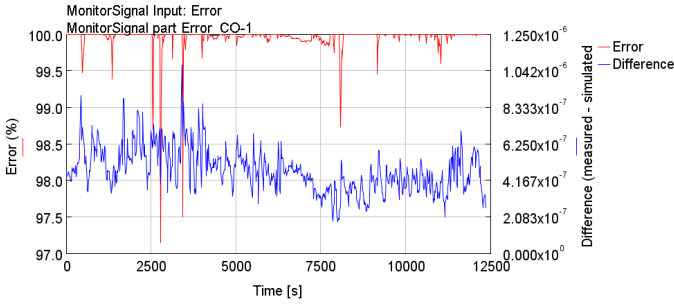

(b) Error of CO

Figure 84: CO simulation with NRTC for DOC+DPF

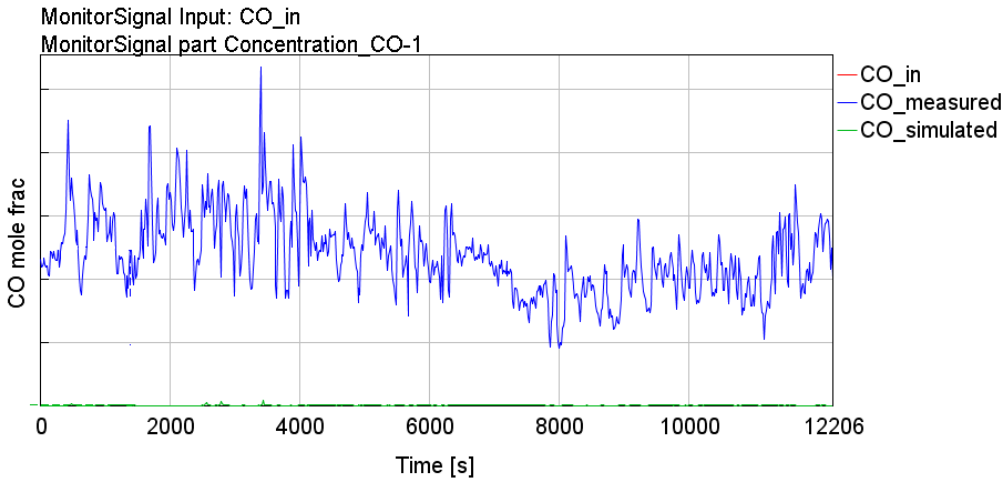

Figure 85: Zoomed CO concentration with NRTC for DOC+DPF

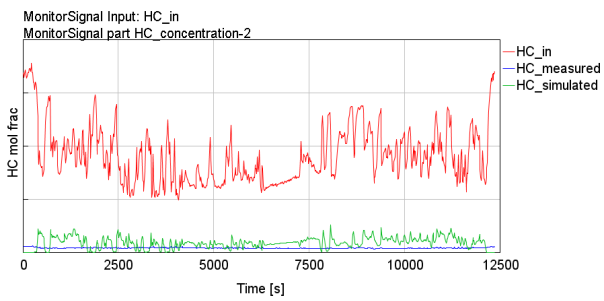

(a) HC

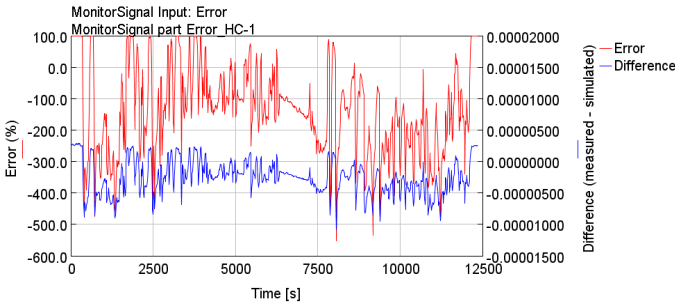

(b) Error of HC

Figure 86: HC simulation with NRTC for DOC+DPF

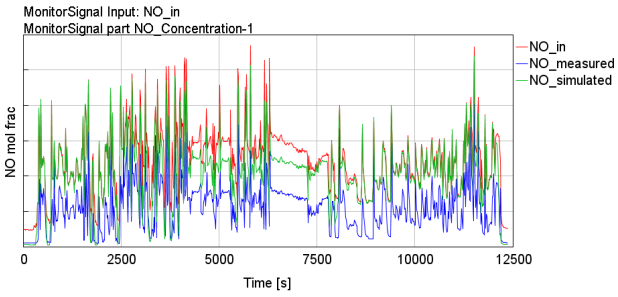

(a) NO

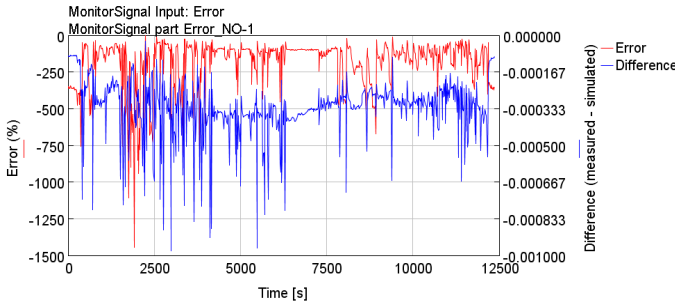

(b) Error of NO

Figure 87: NO simulation with NRTC for DOC+DPF

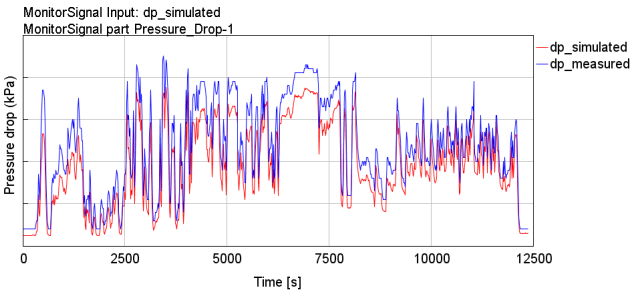

(a) Pressure drop

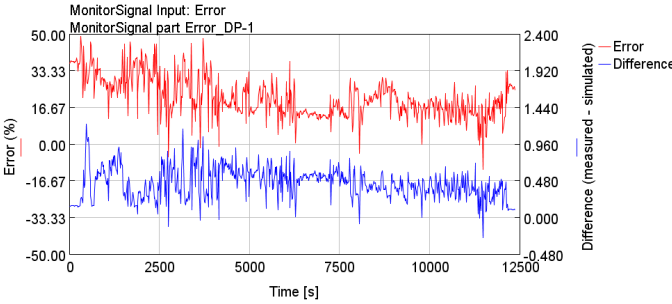

(b) Error of pressure drop

Figure 88: Pressure drop simulation with NRTC for DOC+DPF